BIOCHEMISTRY

# Membrane curvature association of amphipathic helix 8 drives constitutive endocytosis of GPCRs

**Jan Hendrik Schmidt[1]†, Rasmus Herlo[1]†, Joscha Rombach[1], Andreas Haahr Larsen[1], Mikkel Stoklund[1], Mathias Perslev[1], Tommas Theiss Ehler Nielsen[1], Keenie Ayla Andersen[1], Carmen Klein Herenbrink[1], Matthew D. Lycas[1], Aske Lykke Ejdrup[1], Nikolaj Riis Christensen[1], Jan P. Christensen[2], Mootaz Salman[3], Freja Herborg[1], Ulrik Gether[1], Alexander Sebastian Hauser[4], Patricia Bassereau[5], David Perrais[6], Kenneth Lindegaard Madsen[1]***



**Cellular signaling relies on the activity of transmembrane receptors and their presentation on the cellular surface. Their continuous insertion in the plasma membrane is balanced by constitutive and activity-dependent internalization, which is orchestrated by adaptor proteins recognizing semispecific motifs within the receptors' intracellular regions. Here, we describe a complementary trafficking mechanism for G protein–coupled receptors (GPCRs) that is evolutionary conserved and refined. This mechanism relies on the insertion of their amphipathic helix 8 into the inner leaflet of lipid membranes, orthogonal to the transmembrane helices. These amphipathic helices dictate subcellular localization of the receptors and autonomously drive their endocytosis by cooperative assembly and association with areas of high membrane curvature. The strength of helix 8 membrane insertion propensity quantitatively predicts the rate of constitutive internalization of GPCRs. This discovery advances our understanding of membrane protein trafficking and highlights a principle of receptor-lipid interactions that may have broad implications for cellular signaling and therapeutic targeting.**

## INTRODUCTION

Cellular trafficking and sorting processes direct transmembrane proteins (TMPs) to their proper destination within the cell. Consequently, these processes are of fundamental importance for cellular homeostasis, metabolism, and communication. Malfunction results in diseases including cancer, metabolic syndromes, neuropathies, neurodegenerative disease, and psychiatric disorders (*1*).

The transport of TMPs between different cellular compartments is mediated through the action of vesicular membrane carriers. Specificity in trafficking itineraries is achieved by selective sorting of TMP cargo into these carriers, eventually giving rise to differential localizations of TMPs within the cell. This sorting relies partly on semispecific protein-protein interactions between compartment specific adaptor proteins (APs; e.g., AP1-5 and GGAs) and short linear motifs within the cargo TMPs (e.g., FXNPXY and tyrosine- and dileucine-based signals) (*2*, *3*). However, these signals are highly ambiguous and offer little predictive power, leaving critical gaps in our understanding of how individual TMP localization is precisely regulated within cells.

The initial budding and formation of vesicular carriers involves generation of high membrane curvature that serves to recruit specific scaffolding and regulatory cytosolic proteins (*4*, *5*). This mechanism, termed membrane curvature sensing (MCS), is frequently mediated by amphipathic helices (AHs) that insert partially into exposed lipid packing defects in the convex leaflet of curved membranes (*6*, *7*). We hypothesized that AHs in the intracellular termini of TMPs, positioned at the membrane-cytoplasm interface, serve to partition TMPs into areas of high curvature during formation of vesicular carriers, thereby serving as a generic mechanism driving differential forward trafficking of TMPs in the endolysosomal system.

Using G protein–coupled receptors (GPCRs) as example, our data demonstrate that AHs direct constitutive trafficking and redistribution of TMPs with rates quantitatively predicted by their membrane insertion propensity (MIP). We demonstrate that this trafficking mechanism of TMPs, which relies on direct association with highly curved membranes in budding membrane carriers, is fundamentally distinct in terms of kinetics and molecular association from conventional adaptor-based TMP trafficking processes, such as agonist-induced internalization. Moreover, we present data suggesting that MIP of GPCR AHs is conserved across GPCR families and animal species and has been refined during the course of evolution. We refer to this mechanism as trafficking of TMPs by amphipathic motifs (ToTAM) and propose it as a complementary means of cellular sorting and localization to adaptor-based sorting of TMPs.

## RESULTS

### AHs drive constitutive internalization of TMPs

GPCRs constitute the largest family of TMPs in the human genome and include receptors for diverse signaling molecules, such as small-molecule neurotransmitters, peptides, glycoproteins, lipids, nucleotides, and ions (*8*). They control vital physiological functions and represent targets for roughly a third of Food and Drug Administration–approved drugs (*9*). GPCRs consist of seven transmembrane α-helices and a commonly amphipathic eighth helix (H8) that can insert into the cytosolic leaflet of the membrane orthogonal to the transmembrane helices (Fig. 1A) (*10*–*13*). Interactions between H8 and cytosolic APs are known to mediate various trafficking processes, including both agonist-induced and constitutive internalization (*14*).

[1]Molecular Neuropharmacology and Genetics Laboratory, Department of Neuroscience, Faculty of Health and Medical Sciences, University of Copenhagen, 2200 Copenhagen N, Denmark. [2]Department of Immunology and Microbiology, Faculty of Health and Medical Sciences, University of Copenhagen, 2200 Copenhagen N, Denmark. [3]Department of Physiology, Anatomy and Genetics, Wolfson College, University of Oxford, Oxford OX1 3QU, UK. [4]Department of Drug Design and Pharmacology, University of Copenhagen, 2100 Copenhagen, Denmark. [5]Institut Curie, Université PSL, Sorbonne Université, CNRS UMR168, Laboratoire Physico-Chimie Curie, 75005 Paris, France. [6]Université de Bordeaux, CNRS, Interdisciplinary Institute for Neuroscience, IINS, UMR 5297, 33000 Bordeaux, France.
*Corresponding author. Email: kennethma@sund.ku.dk
†These authors contributed equally to this work.

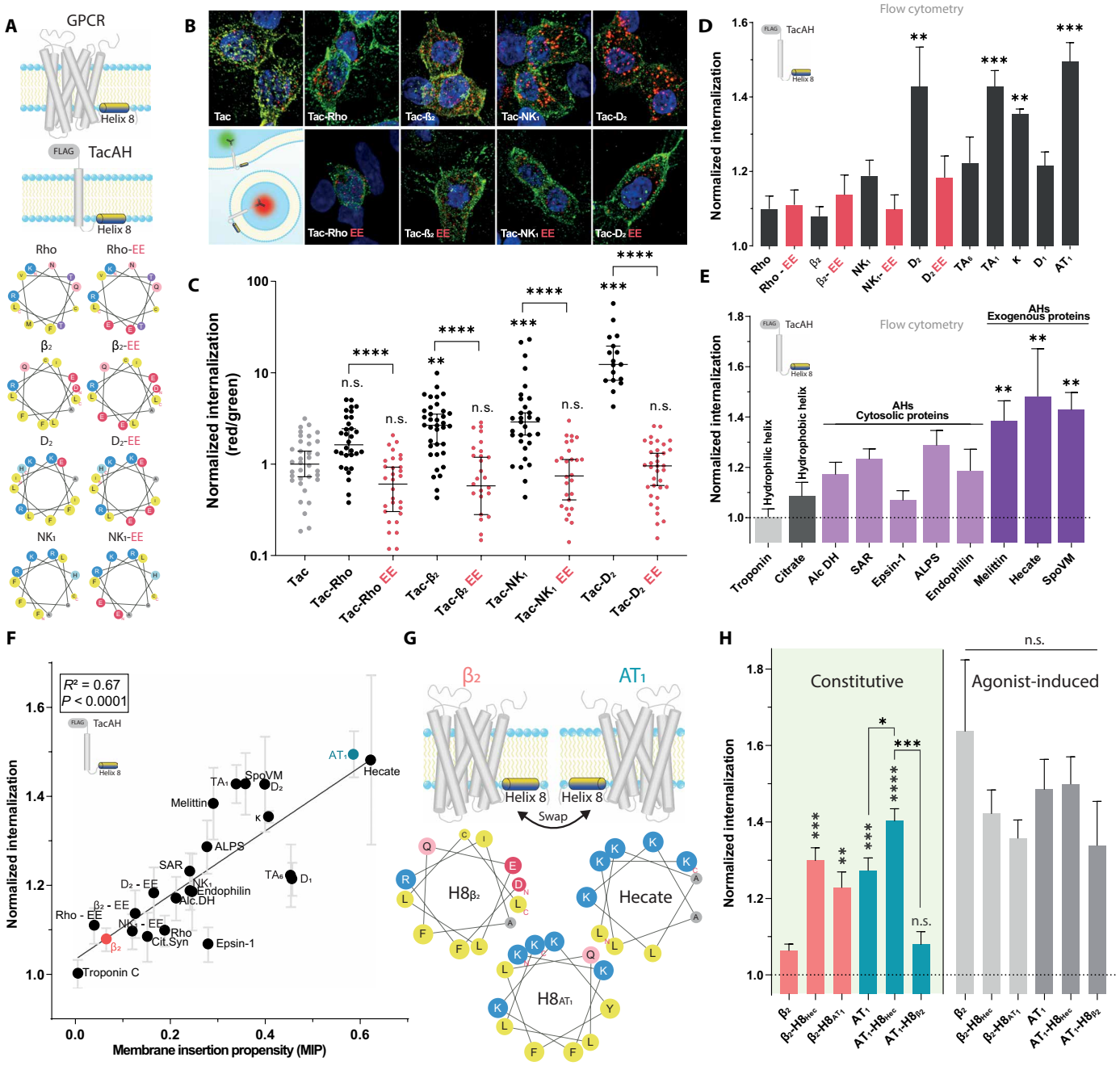


**Fig. 1. AHs in TMPs autonomously drive their endocytosis.** (**A**) Illustration of GPCR H8 sequences transferred to the single TMP Tac for determination of their autonomous endocytic drive alongside mutational disruption of amphipathicity by introduction of negative charges in the hydrophobic face of H8. (**B**) Representative images of human embryonic kidney (HEK) 293 cells transfected with Tac-H8 constructs and subjected to antibody feeding (illustrated in inset, bottom left). (**C**) Quantification of internalization (red/green fluorescence ratio), relative to Tac, from confocal images (every dot represents a cell), $n = 3$. (**D**) Internalization of Tac-H8 constructs assessed by flow cytometry and normalized to Tac. Means ± SEM, $n = 3$. (**E**) Internalization of Tac with AHs from cytosolic proteins or exogenous AHs assessed by flow cytometry. Means ± SEM, $n = 3$. (**F**) Linear correlation ($R^2 = 0.64$, $P < 0.0001$) between MIP of Tac-AH constructs and their respective endocytic rate (relative to Tac). Means ± SEM, $n = 3$. (**G**) Illustration of chimeric H8 GPCRs with swapped part highlighted in helical wheel representations using HeliQuest (*58*). (**H**) Constitutive and agonist-induced (10 μM agonists) internalization rates of chimeric FLAG-tagged GPCR constructs with swapped H8 sequences relative to Tac. Means ± SEM, $n = 3$. n.s., not significant. $^*P < 0.05$, $^{**}P < 0.01$, $^{***}P < 0.001$, and $^{****}P < 0.0001$.

To test our hypothesis, that AHs in the intracellular termini of TMPs can drive their forward trafficking in the endolysosomal system, we tested the autonomous function of H8 in endocytosis. We fused peptide sequences harboring H8 (17 to 18 residues) from a number of well-characterized class A GPCRs [rhodopsin (Rho), β2 adrenergic receptor ($\beta_2$), substance P receptor ($NK_1$), and dopamine D2 receptor ($D_2$)] to the cytosolic C terminus of the internalization inert transmembrane interleukin-2 receptor subunit α, hereafter referred to as Tac (Fig. 1A) (*15*, *16*). The addition of AHs increased internalization of Tac as determined by quantitative confocal microscopy of antibody feeding experiments in human embryonic kidney (HEK) 293 cells (up to 10-fold for Tac-D2) (Fig. 1, B and C). Disrupting the hydrophobic wedge of the AHs by introducing negative charges (Fig. 1A) abrogated this internalization. We recapitulated these findings in HeLa cells (fig. S1). Alanine substitution of cysteines, previously shown to modify trafficking of GPCRs through acylation (*17*), did not further affect internalization in this context (fig. S2).

After confirming the relative internalization rates with high-throughput quantitative flow cytometry (fig. S3) (*18*), we showed that five additional H8s with distinct amphipathic nature, i.e., with high hydrophobic moment, also increased Tac internalization (Fig. 1D). These were H8 from trace amine receptor 1 and 6 ($TA_1$ and $TA_6$), kappa opioid receptor (κ), dopamine D1 receptor ($D_1$), and angiotensin 2 type 1 receptor ($AT_1$) (biochemical parameters outlined in fig. S4). To consolidate and broaden these findings, we also tested non-GPCR helices. Fusion of a hydrophilic helix from troponin (*19*) or the hydrophobic helix from citrate (*20*) did not increase Tac internalization, whereas AHs of several membrane-associated proteins involved in membrane trafficking, including amphipathic lipid packing sensor (ALPS), Sar1, and endophilin A1, but not epsin-1 (*21*, *22*), facilitated internalization (Fig. 1E). Similarly, exogenous AHs, including those from the bee venom Melittin and the bacterial sporulation protein SpoVM as well as the artificial AH Hecate, strongly facilitated internalization of Tac. Together, these findings demonstrate that AHs, diverse in origin and devoid of known adaptor motifs, autonomously increase endocytosis of a TMP. We refer to this mechanism as ToTAM.

## The MIP of AHs quantitatively predicts their effect on TMP internalization

To quantify the propensity of individual AHs to associate with positive membrane curvature, we calculated the hydrophobic moment of AHs and adjusted it by their intrinsic helical propensity (see Materials and Methods) (*23*). The resulting value, MIP, correlated with empirical measures of membrane association strength as determined by liposome binding to peptides on a SPOT array (fig. S5). Furthermore, plotting internalization of the AH-fused Tac constructs as a function of MIP yielded a strong correlation irrespective of the origin of the AHs (Fig. 1F), demonstrating that AHs drive internalization of TMPs in a predictive manner. In comparison, net charge and hydrophobicity demonstrated much lower predictive power of internalization rate on their own (fig. S6, A and B). In absolute terms, AHs increased internalization from a basal level of 20% of Tac over a 30-min period to a complete (100%) turnover of Tac-AHs for the strongest AHs (fig. S7).

## The amphipathic nature of H8 drives constitutive endocytosis of full-length GPCRs

To address the endocytic function of H8 in context of full-length receptors, we focused on $\beta_2$ and $AT_1$, which contain H8s with pronounced differences in their autonomous endocytic drive (Fig. 1F, red and blue, respectively). We made chimeric constructs by interchanging their H8s (Fig. 1G) and assessed their internalization. In concordance with the autonomous drive of their H8s, $AT_1$ displayed significantly higher constitutive internalization than $\beta_2$, and this pattern was fully reversed by swapping their helices (Fig. 1H and fig. S8). Furthermore, the introduction of the synthetic, potent AH Hecate (Fig. 1G) gave rise to an even higher internalization rate than that of $AT_1$ H8, in context of both $\beta_2$ and $AT_1$. In contrast, internalization in presence of agonist was robust for all constructs irrespective of AH (Fig. 1H and fig. S8). Further, while constitutive internalization scaled linearly with expression, agonist induced internalization for the H8-containing constructs deviated from linearity consistent with saturation of adaptor-based internalization machinery (fig. S8) (*24*). This suggests that MIP of H8 drives constitutive, but not agonist-induced, internalization of GPCRs.

## AHs in TMPs regulate their cellular distribution at steady state

To assess how AHs might affect the steady-state distribution, we chose five Tac-AH constructs, spanning from low to high MIP values for further investigation. Permeabilized immunocytochemistry analysis revealed robust total expression of all constructs with Tac-$AT_1$ and Tac-Hecate showing increased signal compared to Tac (fig. S9). Structured illumination microscopy did not reveal obvious differences in steady distribution (fig. S10). To obtain better quantitative insight into the steady-state distribution of TMPs, we performed a proximity biotinylation approach and fused the small (26.4 kDa) biotin ligase BioID2 (*25*) to the C-terminal end of the TAC-AH constructs (Fig. 2A). Western blot analysis confirmed expression of proteins of the expected size (62 kDa, lower band unglycosylated) and further suggested a reduced glycosylation (>75 kDa, upper band) with increasing MIP (Fig. 2B, top), similar to constructs without BioID2 (fig. S11). The BioID2-fusion constructs recapitulated ToTAM-driven internalization as assessed by quantitative confocal microscopy (Fig. 2B, bottom; and fig. S12, A and B). Following a 24-hour incubation with excess biotin, we performed affinity purification of the biotinylated proteins to assess their differential association with the AH-containing BioID2-fusion constructs by quantitative label-free liquid chromatography–tandem mass spectrometry (LC-MS/MS) (*25*). We identified a total of 2569 unique proteins and grouped them by subcellular localization according to a negative matrix factorization approach previously applied to proximity biotinylation experiments (*26*) and evaluated relative enrichment of proteins found in TacAH-BioID2–transfected cells versus mock (pcDNA). Proteins belonging to the endolysosomal pathway were among the most enriched (fig. S12C), validating the proximity labeling strategy. Among the subcellular compartments belonging to the endosomal system, only "plasma membrane" exhibited significantly differential enrichment across the BioID2-fusion proteins, revealing a strong negative association with increasing MIP values consistent with reduced maturation and increased internalization (Fig. 2C). Weaker, nonsignificant trends were observed for the remaining endolysosomal compartments.

Upon analysis of the total variance of the data by principal components analysis (PCA), we observed a MIP-dependent distinction of protein labeling intensities by TacAH-BioID2 constructs (Fig. 2D). We next asked whether MIP value was associated with any individual proteins. Linear regression analysis of all identified proteins highlighted a subset of proteins that showed strong positive correlation

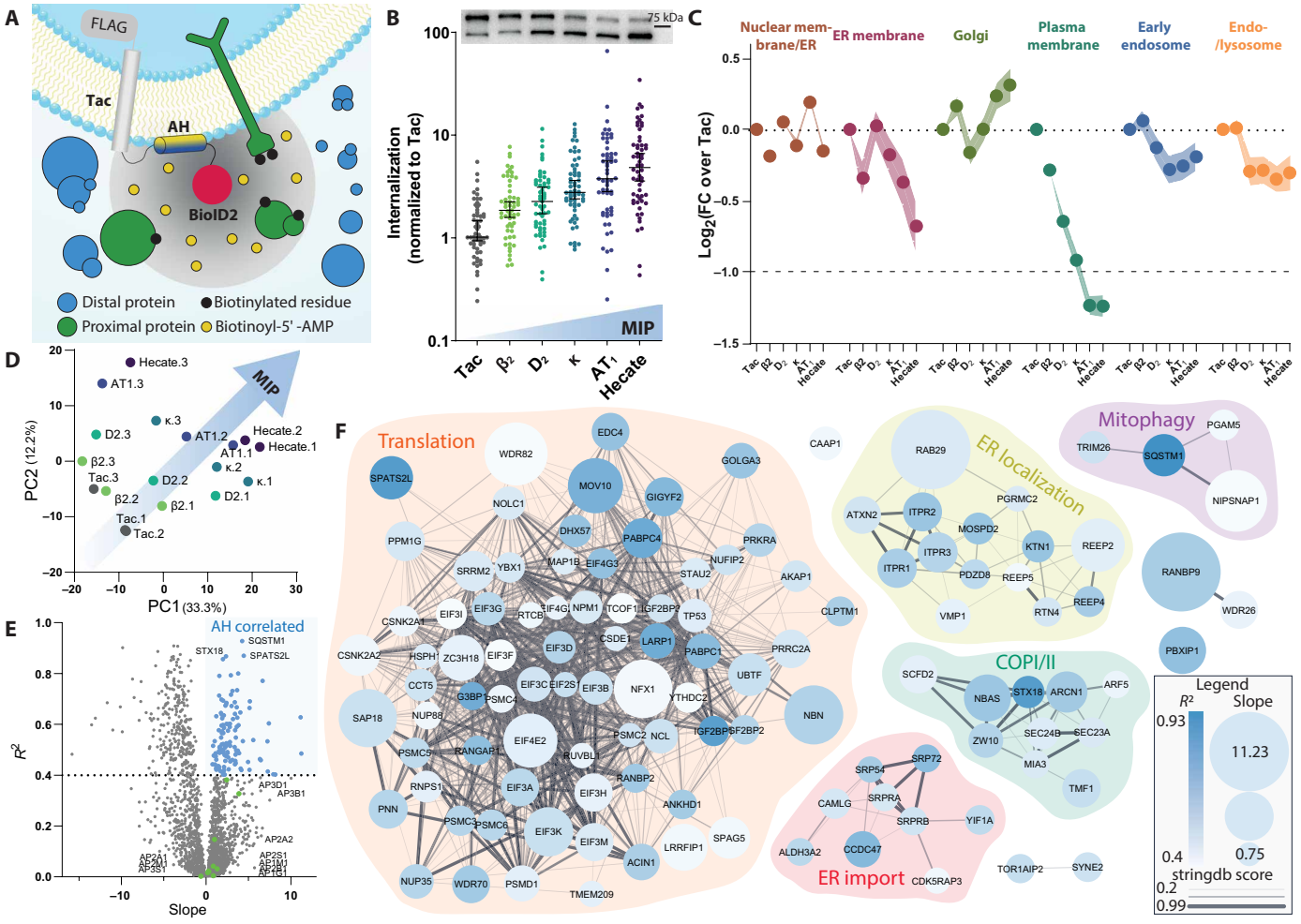


**Fig. 2. Increasing MIP drives association with the biosynthetic pathway and away from the plasma membrane.** (**A**) Schematic of proximity biotinylation assay with BioID2. (**B**) Top: Western blot (M1 ab) of Flag-Tac AH-BioID2 constructs transfected in HEK293 cells showing mature proteins [high molecular weight (MW) band] and immature protein (low MW band). Bottom: Quantification of internalization of Flag-Tac AH BioID2 constructs from confocal images (every dot represents a cell, compiled from three independent experiments). (**C**) Differences in label-free quantification (LFQ) values for indicated constructs versus basal levels (pcDNA) normalized to Tac compiled for all identified proteins belonging to endolysosomal compartments of MMF grouping in (*26*). FC, fold change. (**D**) Principal components analysis (PCA) biplot showing spread of MS samples along principal component 1 (PC1) and PC2 indicating a MIP-driven separation. (**E**) Volcano plot highlighting slope and $R^2$ values of linear correlations for each identified protein with MIP of the Tac-AH-BioID2 constructs. Protein correlating with MIP (slope > 0 and $R^2$ > 0.4) highlighted in blue. Identified AP complex subunits (indicated in green). (**F**) STRING protein network analysis of the proteins identified as MIP correlated in (E) in functional groups based on database annotations.

[coefficient of determination ($R^2$) > 0.4] with MIP (indicated in light blue). Of note, none of the identified AP complex subunits (indicated in green) fulfilled these criteria (Fig. 2E). Protein network analysis of the strongly MIP-correlated subset revealed several tightly connected clusters annotated as related to translation, endoplasmatic reticulum (ER) localization, ER import, COPI/II (coat protein complex I/II) complex, and mitophagy (Fig. 2F). Plotting all identified core proteins of the COPI and COPII complexes revealed an overall increased abundance with MIP (fig. S12, D and E). Together, these findings suggest a MIP-dependent steady-state enrichment of TMP within the early biosynthetic pathway as well as a depletion at the plasma membrane.

## ToTAM is associated with clathrin

Because we found no significant associations between MIP and any classical or putative endocytic adapter proteins, we asked more qualitatively how the Tac-BioID2 constructs differentially labeled established components of the endocytic machinery similar to the analysis for the COPI and COPII complexes. The MIP of the expressed Tac-AHs did not significantly affect the enrichment of actin or dynamin (Fig. 3A), consistent with a low impact of treatment with the actin polymerization inhibitor latrunculin A, 5-[*N*-ethyl-*N*-isopropyl] amiloride (EIPA), and Dyngo-4A on internalization of Tac-AHs (fig. S13, A to C). In comparison, adenosine 5′-triphosphate depletion resulted in a relative reduction of internalization for all constructs (fig. S13, D to F), indicating involvement of energy-dependent processes in ToTAM.

Next, we addressed association of the Tac-BioID2 constructs with components of specific endocytic pathways. Key proteins of clathrin-mediated endocytosis (CME) (*27*), particularly clathrin and EPS15, were enriched for all Tac-AHs (Fig. 3B). On the other hand, identified components of the CLIC/GEEC pathway and caveolae (*28*, *29*) were consistently less enriched with increasing MIP of the

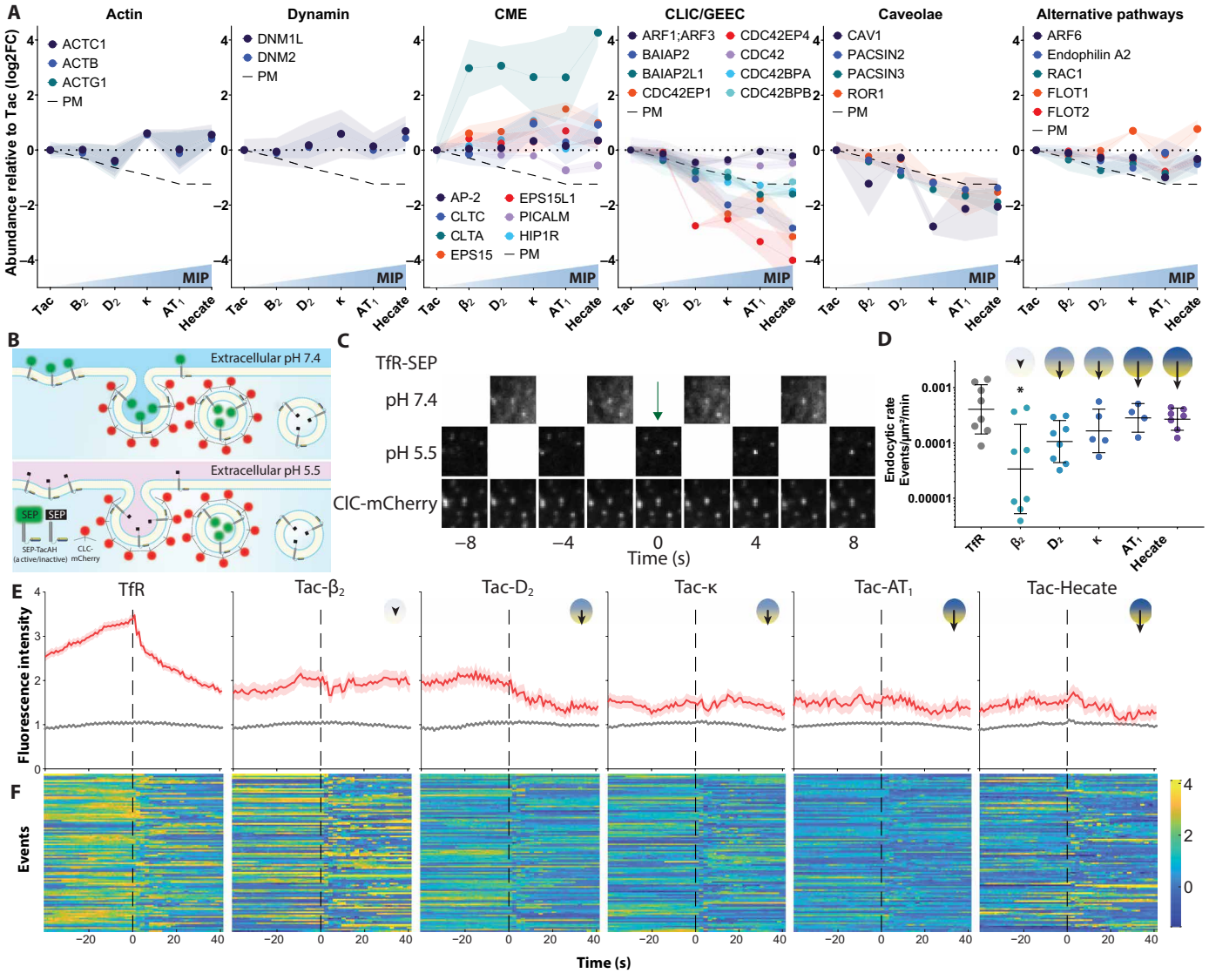


**Fig. 3. ToTAM associates with CME machinery in a noncanonical manner.** (**A** and **B**) Absolute difference in LFQ values (normalized to Tac) of identified actin and dynamin subunits (A) and selected identified proteins associated with CME, CLIG/GEEC, caveolae, and other endocytic pathways (B). (**C**) Schematic of (ppH-TIRFM) protocol enabling definition of time of scission for individual endocytic events. (**D**) Images of representative endocytic event from ppHTIRFM experiments of superecliptic pHluorin (SEP)–tagged transferrin receptor (TfR) together with clathrin light chain (CLC)–mCherry. (**E**) Endocytic event rate for the five different SEP-TacAH constructs compared to TfR-SEP. Statistical analysis using Kruskal-Wallis multiple comparisons test. (**F**) Top: Average of individually normalized CLC-mCherry traces for TfR-SEP and 5 SEP-TacAH constructs. Bottom: Heatmaps of normalized individual CLC-mCherry traces pre- and postscission. $n = 5$ to 10 cells (846 to 2797 events) per condition. $^{*}P < 0.05$, $^{**}P < 0.01$, $^{***}P < 0.001$, and $^{****}P < 0.0001$.

Tac-AHs. Last, enrichment of proteins involved in alternative endocytic pathways, including Arf6, Rac1, endophilin A2, and flotillins [FLOT1 and FLOT2; (*30*)], was relatively independent of MIP. Taking into account the reduced surface expression of Tac-BioID2 constructs as a function of MIP (dashed line), we interpret that the AHs likely do not actively drive sorting away from CLIC/GEEC or caveolae, but that AHs potentially sort TMPs toward alternative endocytic pathways involving Arf6, Rac1, endophilin A2, and flotillins, in addition to CME.

Grouping all identified CME-associated proteins according to temporally defined modules (*31*), we observed no marked increase in association with nucleation and assembly, neck constriction or scission, and movement modules, while proteins involved in uncoating as well as endosome fusion were enriched for all AHs (fig. S14A). Notably, proteins of the nucleation and formation module that showed increased abundance, including clathrin and EPS15, represented a group that has been shown to be continuously associated with CME events until uncoating (*27*). To test the functional effect of such association, we overexpressed a dominant negative EPS15 (Δ95-295). Expression did not abolish the MIP-induced internalization but did confer an expression dependent decrease in internalization for all constructs (although not significant for Tac and Tac-Hecate). Conversely, overexpression of the dominant negative dynamin 2 (K44A) did not compromise internalization (fig. S15).

EPS15 is known to recruit ubiquitinated cargo to endocytic sites (*32*). In accordance, we detected minor increases in ubiquitin binding proteins of the ESCRT machinery and E3 ubiquitin ligases (fig. S14, B and C) (*33*), as well as the ubiquitin-receptor SQSTM1 (p62) as the top hit among MIP correlated associations (Fig. 2, E and F). This suggests an interaction with the ubiquitin machinery, despite no evident ubiquitination of the Tac-AH constructs (Fig. 2B). Together, ToTAM associates with CME and likely with components of alternative pathways while seemingly avoiding GLIC/GEEC and caveolae in addition to the downstream ubiquitin machinery.

### ToTAM is temporally uncoupled from classical CME

To directly evaluate the trafficking dynamics of Tac-AH constructs and the CME structures that they associate with, we turned to pulsed pH (ppH) total internal reflection microscopy (TIRFM) assay (*34*) using superecliptic pHluorin (SEP)–tagged constructs coexpressed with mCherry-tagged clathrin light chain (CLC) (Fig. 3, C to F, and fig. S16) using the bona fide adaptor-mediated endocytosis of the transferrin receptor (TfR) as reference. Corroborating the previous findings, the number of endocytic events increased by almost an order of magnitude with increased MIP of the AHs, approaching the rate of TfR for the strongest helices (H8 from $AT_1$, and Hecate) (Fig. 3E). Exocytosis increased correspondingly, suggesting efficient intracellular sorting to recycling endosomes (fig. S17). CLC fluorescence intensity traces associated with TfR endocytic events (red line showing averaged traces) displayed a typical profile with gradual accumulation until point of scission followed by a rapid decrease after scission (Fig. 3F). This distinct profile was gradually lost with increasing MIP of the Tac-AH constructs indicating that scission is temporally uncoupled from classical CME, although some spatial association with CLC was retained for all constructs (red line is above the gray line showing the average level of CLC away from endocytic events). Examination of individual normalized traces displayed a range of CLC recruitment profiles (Fig. 3F, bottom, and fig. S18). PCA revealed a decreasing fraction of traces similar to the typical TfR-associated CLC profile for Tac-AHs with increasing MIP (fig. S19). Conversely, an increased fraction of events displayed accumulation of CLC immediate postscission. In summary, increased MIP directs ToTAM toward bulk association with CME core machinery at the expense of other endocytic machineries while simultaneously decreasing the temporal synchronization and coordination with clathrin dynamics.

### ToTAM involves accelerated endocytic maturation and scission

Next, we analyzed the recruitment dynamics of the SEP-Tac-AH constructs themselves before scission (Fig. 4A). While SEP-TfR accumulated at a steady rate during vesicle formation (*35*), the AH-linked profiles showed fast and accelerating kinetics with increasing MIP of AHs. Fitting these profiles with a logistic equation indicated an increasingly cooperative clustering mechanism consistent with an autonucleating function underlying ToTAM (Fig. 4B).

To determine whether this effect translates into a generalized increase in maturation rate of endocytic structures, we performed transferrin uptake in cells expressing the Tac-AH constructs. This demonstrated a strong and MIP-dependent increase in transferrin uptake in trans (Fig. 4C). Cargo load of individual endocytic events determined from the ppH-TIRFM experiments (pH 5.5 fluorescence at the time of scission) was decreased with increasing MIP of AHs (Fig. 4D), whereas quenching rates as a result of endosomal acidification increased with MIP of AHs (Fig. 4E). Relating the cargo load to the acidification rates as a measure of endosome size [three-dimensional (3D) volume] further suggests an increased cargo density with increasing MIP of AHs (fig. S20). Together, we find that ToTAM is characterized by numerous, fast, small, and cooperative endocytic events with the potential to accelerate overall trafficking rates.

### ToTAM associated with high membrane curvature during endocytosis

The temporal uncoupling with canonical endocytic machinery as well as the cooperative, high-density recruitment and the inductive properties of ToTAM collectively point to an underlying autonomous and recursive mechanism, consistent with concurrent MCS and induction, which is a common characteristic of AH association with lipid membranes. We therefore investigated the MCS properties of Hecate (the AH tested with highest MIP) in a buckled membrane system using molecular dynamics simulation. This simulation predicted a curvature sensitive membrane sorting (Fig. 5, A and B), akin to previous findings for ALPS (*36*). To experimentally confirm association with high membrane curvature, we incubated BODIPY-TR–labeled giant unilamellar vesicles (GUVs) (red) with Oregon green 488–labeled Hecate peptide (green). Consistent with the cooperative clustering observed in the ppH–total internal reflection fluorescence (TIRF) experiments, the Hecate peptide occasionally formed bulging microdomains on GUVs in the absence of manipulation indicative of membrane curvature induction (Fig. 5C).

Next, we pulled tethers from GUVs preincubated with OG488-Hecate to generate a high membrane curvature domain and observed a significant enrichment of the Hecate peptide on the tether (peptide on tether relative to GUV) (Fig. 5, D and E). A control peptide with similar charge but reduced helical propensity and MIP of the helix did not bind to GUVs (fig. S21). Given this in vitro evidence, we next tested whether the Tac-AH constructs displayed membrane curvature association at the plasma membrane of cells. To assess the size and curvature of the endocytic budding structures encompassing the cargo before scission, we antibody labeled surface-expressed Tac-AHs for 3D-dSTORM imaging and identified protein clusters using DBSCAN analysis (Fig. 5F and fig. S22). While the median radius of clusters was 100 nm for Tac, consistent with the size of clathrin-coated pits (*37*), cluster sizes were consistently smaller with increasing MIP of AHs (Fig. 5G). We further extracted the number of localizations per cluster, enabling us to plot protein densities of individual budding structures as a function of size. In our previous studies, we have demonstrated and rationalized by modeling that the MCS by amphipathic insertion into lipid membrane defects gives rise to a log-log linear relationship (*6*). The averaged cargo densities for the different size bins gradually approached a linear relationship (indicated by the dashed line) with increasing MIP of the AHs (Fig. 5H). Moreover, the negative slope, which indicates the degree of MCS, nominally increased as a function of the MIP of the AH (Fig. 5I) (*6*). In summary, we propose that ToTAM mechanistically serves both to localize cargo to endocytic pits and to facilitate the membrane curvature induction and possibly scission of these pits to drive endocytosis.

### Mapping of MIP in the C termini of human GPCRs

To characterize the membrane association of C termini across the full range of Human GPCRs, we developed the liposome binding

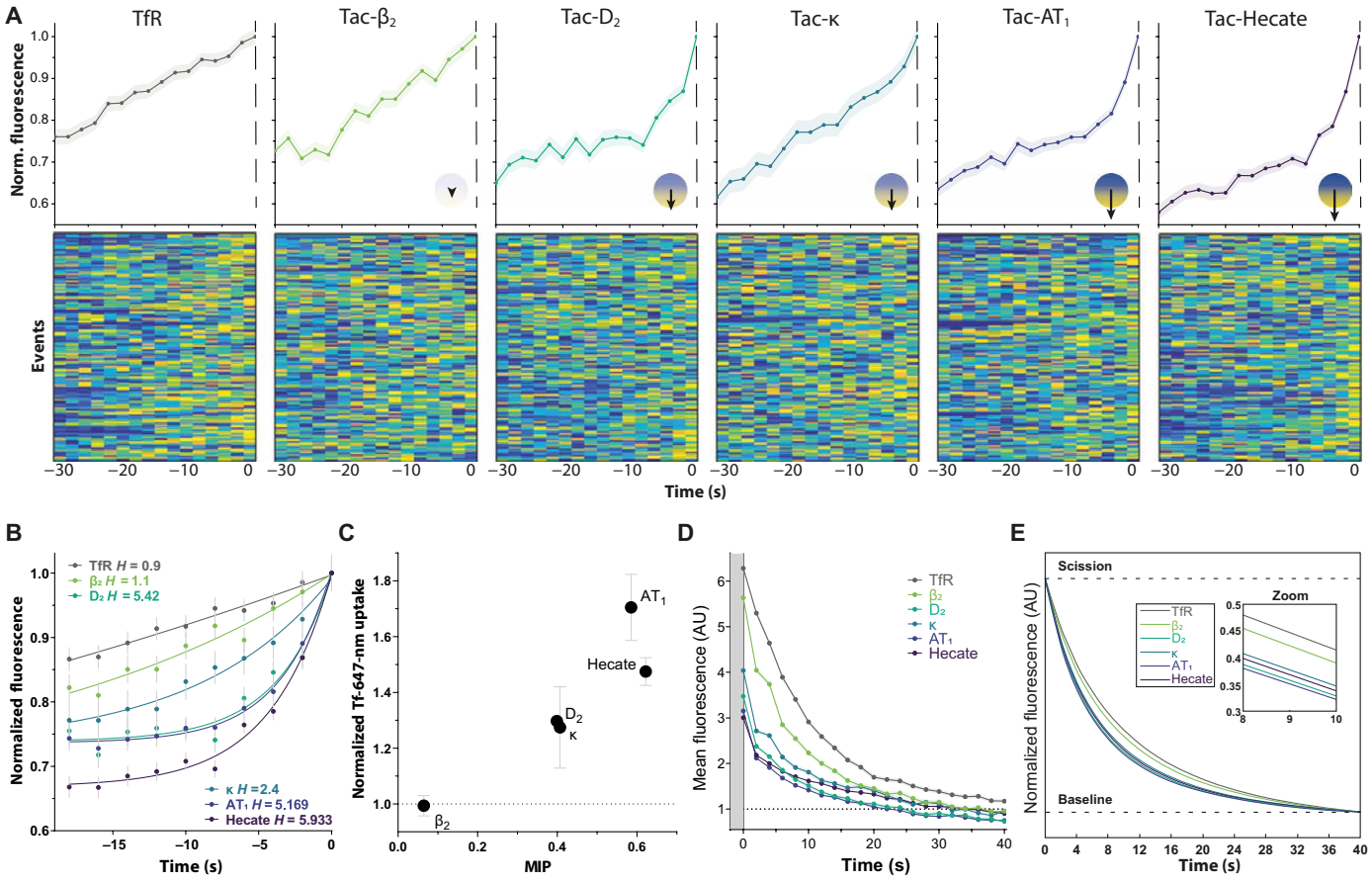


**Fig. 4. ToTAM involves accelerated endocytic maturation and scission.** (**A**) Top: Average of individually normalized pH 7.4 TfR-SEP and SEP-TacAH fluorescence intensity traces building up to point of scission (time = 0). Bottom: Heatmaps of normalized individual SEP-fluorescence profiles at pH 7.4 of TfR-SEP and SEP-TacAH constructs before scission. $n = 5$ to 10 cells per condition and $n = 518$ to 2367 total traces. (**B**) Nonlinear regression fits of averaged normalized pHluorin traces up to point of scission. $H$ is the Hill coefficient. (**C**) Effect of TacAH constructs on AF647-labeled transferrin endocytosis in trans by flow cytometry. (**D**) Averaged fluorescent traces measured at pH 5.5 in cell populations expressing either of the six indicated SEP-TacAH constructs. Absolute values shown postscission ($t = 0$). (**E**) Average traces from (D) are normalized to initial fluorescence observed at time of scission ($t = 0$) and fitted to the "Acidification Kinetics Function" (see Materials and Methods). Fits shown for all six SEP-TacAH constructs with TfR eliciting slowest acidification kinetics, while $AT_1$ elicits the fastest acidification kinetics. AU, arbitrary units.

SPOT assay (fig. S5) into a large-scale chip array format using consecutive 16-nucleotide oligomer peptides with a two–amino acid offset (Fig. 6, A and B). Reconstruction of binding profiles from individual peptide binding values revealed confined membrane binding regions of different strength as illustrated by the C-terminal regions of rhodopsin, $\beta_2$ and $AT_1$ (Fig. 6C). These regions overlap with the H8 region as indicated by their high MIP values. All receptor profiles are displayed in fig. S23. Averaged membrane binding profiles for each of the GPCR families confirmed this pattern for rhodopsin (disregarding olfactory receptors) as well as for secretin and frizzled families, albeit with membrane binding extending slightly further away from the TM region for the latter. Membrane binding was less pronounced for the remaining families and absent from the glutamate receptor family (Fig. 6D). Moreover, these binding profiles are in good agreement with the conservation of amphipathic periodicity in H8 across the GPCR families (fig. S24A) (*38*). Clustering of binding profiles of C termini from individual receptors revealed an unexpectedly large group of GPCRs (cluster 1) without membrane binding (Fig. 6, E and F) that, thus, are unlikely to affect internalization of their respective receptors through ToTAM. Several of these cluster 1 receptors are from the glutamate receptor family in agreement with the low average profile of the family (Fig. 6D). However, many additional receptors belonging to other families and without any clear evolutionary origin also show no membrane binding, suggesting that mechanisms other than ToTAM regulate the trafficking and localization of these receptors. Notably, this is true for many receptors belonging to the rhodopsin family (figs. S23 and S24B). Clusters 2 to 5 showed membrane binding profiles consistent with membrane proximal H8, albeit with different intensities of the binding within each cluster and increasing length and distance from TM7 going from clusters 2 to 5 (Fig. 6, D and E, and fig. S23). Last, cluster 6 contained a wide range of different membrane binding profiles, which are more distant from TM7 and/or contain multiple membrane binding sites.

We did not observe a significant enrichment of individual clusters within GPCR receptor families (fig. S24B) or specific tissues (fig. S24C). However, functional enrichment analysis within the studied GPCRs using Gene Ontology (GO) terms revealed a significant enrichment of receptors located to endolysosomal membranes for the bona fide H8 clusters (clusters 2 to 5), while nonbinding

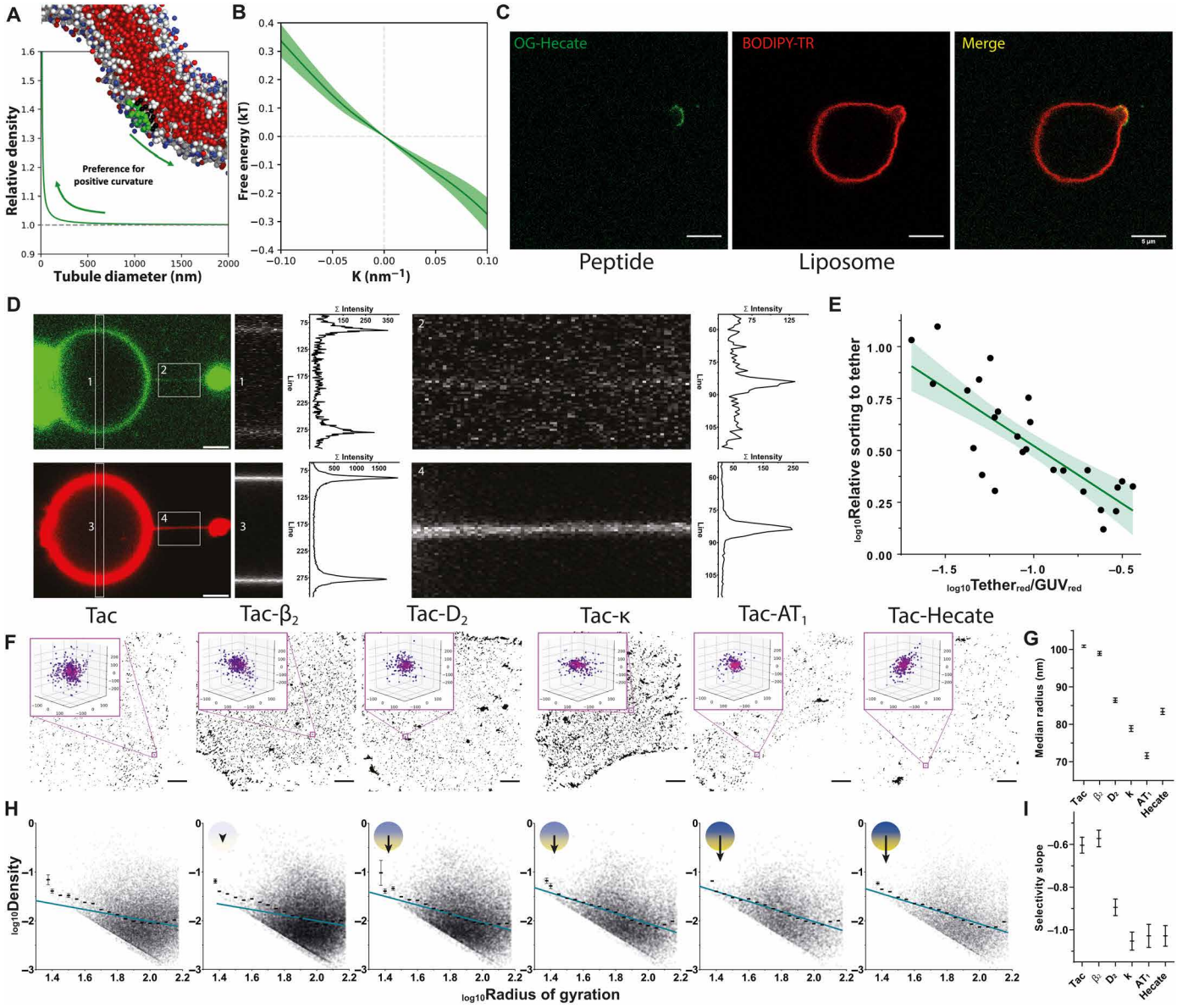


**Fig. 5. ToTAM involves association with high membrane curvature during endocytosis.** (**A**) Relative protein density (Hecate peptide) as a function of tubule diameter determined in buckled membrane MD analysis indicating a strong preference for positive curvature. (**B**) Free energy from (A) as a function of membrane curvature. (**C**) Representative images of Oregon Green 488–labeled Hecate (green) bound to free floating BODIPY-TR–labeled GUVs (red), revealing selective organization of peptides in deformed microdomain structures on the GUVs. Scale bars, 5 μm. (**D**) Tethers pulled from GUVs (red) preincubated with Oregon Green–labeled Hecate peptide (green). Insets 1 and 3, zooms of GUV and summed intensity profile. Insets 2 and 4, zooms of tether and summed intensity profile. (**E**) Quantification of the relative sorting to the tether as a function of relative size of the tether ($Tether_{red}/GUV_{red}$). (**F**) Representative 3D-dSTORM images of FLAG-Tac and five FLAG-TacAH constructs after surface labeling with Alexa Fluor 647–conjugatedM1 α-FLAG antibody. Scale bars, 5 μm. Insets show representative single clusters color coded for localization density. (**G**) Average size of clusters for the individual constructs, median ± 95% CI, $n = 6$. (**H**) Logarithmic relationship of cluster size and cargo density (FLAG-Tac-AH). Black bars show binned averages ± SEM, and the blue line represents a linear fit of the data. Better adherence of the fit to the binned averages indicates curvature dependent sorting for Tac-AH constructs with high MIP. (**I**) Selectivity slope (i.e., curvature sensitivity) derived for linear fits with error on log-log plots of the data in (H) (see fig. S22).

receptors (cluster 1) are associated with disc-like membranes or membranes with topologies that restrict membrane insertion (photoreceptor discs and exosomes, respectively) (fig. S25A). Cluster 6 receptors showed a weak association with caveola and growth cones, although driven by a relatively low number of proteins. A wide range of both molecular function and biological process (BP) terms were associated with all clusters (fig. S25, B and C), leading us to perform a semantic similarity GO term enrichment analysis of the significant BP terms (fig. S25D). Consistent with the enrichment of cluster 1 in photoreceptor discs, we see a strong association with light related BP terms. Clusters 2 to 5 show the strongest association with synaptic transmission, particularly driven by receptors with membrane proximal H8 (cluster 2), while the longer and more distal H8 of cluster 5 associates with cellular differentiation processes. Last, we find that receptors

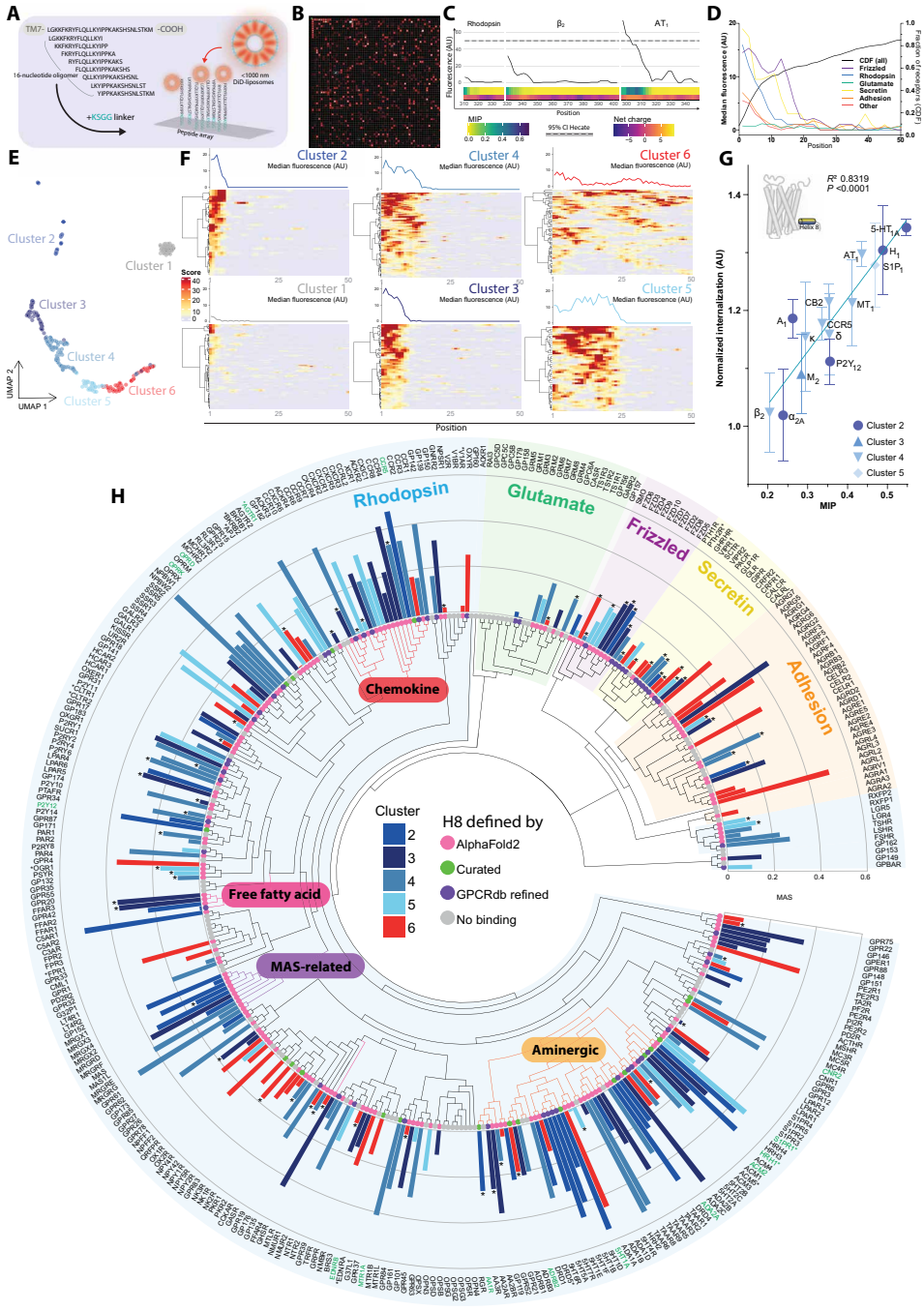


**Fig. 6. Proteome-wide characterization of C-terminal membrane interactions in GPCRs and their role in constitutive endocytosis of GPCR.** (**A**) Schematic of chip array for scanning of liposome binding strength throughout the full range of human GPCR C termini. Individual peptides are randomly positioned on the chip. (**B**) Representative image of fluorescent signal from bound liposomes on enlarged area of array. Regular pattern in top left corner is control Hecate peptide. (**C**) Compiled binding profile of the C termini of rhodopsin, $\beta_2$, and $AT_1$ along with corresponding MIP and net charge values (below). CI, confidence interval. (**D**) Average liposome binding profiles of peptide sequences corresponding to 16–amino acid stretches of GPCR C termini split by GRAFS family (left *y* axis) and cumulative distribution function of all human GPCR C termini (right *y* axis) starting at 16 amino acids. (**E**) UMAP-based clustering of all human GPCR C termini based on position and strength of liposome binding. (**F**) Heatmaps of all individual GPCR C-terminal liposome binding profiles within the six clusters and profile plots of the median fluorescence intensity (line above) (for detailed view, see fig. S23). (**G**) Linear correlation ($R^2 = 0.83$, $P < 0.0001$) between MIP of H8 from clusters 2 to 5, based on sequences (fig. S27) in pharmacologically relevant GPCRs and their respective endocytic rate (relative to Tac) determined by flow cytometry (*39*). Means ± SEM, $n = 3$. (**H**) Circular phylogenetic tree of human GPCRs based on sequence homology and divided into GRAFS families and clusters, alongside the corresponding calculated MIP based on H8 from either refined representative structures as annotated on GPCRdb (purple) (*11*), AlphaFold2 prediction (magenta) (*59*) or manually curated. Receptors used in (G) are highlighted by green, and receptors described as mechanosensitive (*45*) are highlighted by asterisks (name). GPCRs from cluster 1 (no binding) in gray. Receptors with a structural H8 predicted longer than 20 amino acids marked with asterisk (bar). AU, arbitrary units. CDF, cumulative distribution function.

of cluster 6 associate with terms related to peripheral, cardiovascular regulation (fig. S25D).

### MIP of H8's predicts constitutive internalization of human GPCRs

The experimentally derived membrane binding profiles enabled us to delineate bona fide membrane binding H8s (clusters 2 to 5) and calculate MIP values for these regions (fig. S26). We previously characterized the constitutive internalization of a range of pharmacologically relevant GPCRs (*39*) and here asked whether this internalization could be explained by MIP values of the regions defined by their membrane binding profiles. Constitutive internalization significantly correlated with MIP values (clusters 2 to 5) (Fig. 6G), demonstrating that the amphipathic nature of H8 can quantitatively predict constitutive endocytosis of full-length GPCRs. Other biophysical measures, alternative to MIP, failed to explain constitutive internalization (fig. S27, A to C). Consistent with the lack of effects of H8 substitution on agonist induced internalization (Fig. 1H), MIP did not correlate with agonist-induced internalization (fig. S27D). The complex membrane binding profiles of cluster 6 precluded extraction of MIP values, predictive of constitutive internalization (fig. S27E). MIP is not significantly related to β-arrestin recruitment or reported G protein coupling (fig. S28, A and B). Together, these results indicate that the MIP of H8 selectively predicts constitutive internalization across this functionally important and structurally well-characterized subset of GPCRs.

Given the functional importance of constitutive internalization for dynamic surface expression of GPCRs, we utilized MIP of H8 as a proxy to map predicted internalization rates across all nonodorant GPCRs belonging to clusters 2 to 5 by their phylogenetic relation (Fig. 6H and fig. S27F) demonstrating high diversity within families of receptors, even for receptors with high homology such as C5AR1/2, MRGRE/G, OPRD/M, and TAAR2/3 within the rhodopsin family, as well as AGRL1/2 and AGRB1/2/3 within the adhesion receptor family. We also note that secretin and frizzled receptors largely contained a H8 predicted or found to be longer than 20 residues and the functional significance of this remains to be explored. Mapping the receptors by physiological ligands (GPCRdb) (fig. S29) (*40*) emphasized high MIP values within receptors for biogenic amines (serotonine, acetylcholine, noradrenaline/adrenaline, dopamine, and histamine), chemokine receptors, and marker-assisted selection (MAS)-related receptors as well as free fatty acid receptors, alongside individual receptors such as NPBW2 and C5AR1. MIP in GPCRs associated with fast endophilin-mediated endocytosis, which mediate endosomal signaling or function as mechanosensors, displays H8 MIP value distributions that do not deviate significantly from average H8 MIP for all GPCRs (clusters 2 to 5). On the other hand, GPCRs associated with primary cilia, which exhibit topologies with an inverse curvature to endocytic structures, display H8 sequences with significantly lower MIP (fig. S28C). Conversely, GPCRs expressed by viruses, which are known to elicit high constitutive internalization (*41*), mostly have high MIP values of their H8.

### MIP is evolutionary conserved across distant organisms

To assess potential functional conservation of high MIP of H8, we used available data from UK Biobank on naturally occurring variants in human GPCRs. While the cost of individual amino acid substitutions was similar in the H8 region compared to the remaining part of the C termini (Fig. 7A), the frequency of nonsynonymous natural variants was significantly lower within H8s (Fig. 7B). When analyzing differences in MIP resulting from these naturally occurring variants, we found that the observed substitutions give rise to a more conserved MIP than substitutions not observed (Fig. 7C). Last, the frequency of natural variants within H8 for individual receptors declines with increasing MIP, emphasizing the functional conservation of high MIP (Fig. 7D).

Last, we assessed the evolutionary origin and refinement of MIP in H8 of GPCRs. Using the membrane binding array, we found that GPCR C termini from evolutionary distant organisms, including *Caenorhabditis elegans*, *Drosophila Melanogaster*, and *Saccharomyces Cerevisiae*, show membrane binding profiles akin to H8 in human GPCRs (clusters 2 and 3) as well as nonbinding (cluster 1) and more complex binding profiles (clusters 4 and 5) (Fig. 7E and fig. S30). This enabled us to address evolutionary refinement by aligning H8 sequences, as defined in human GPCRs, across species back to their Ecdysozoa counterparts (Fig. 7F). Individual receptors generally show strong conservation of MIP throughout evolution as indicated by the color preservation across the evolution for individual receptors as well as the overall preservation of MIP ranking from yellow to purple across species. The relative variation across species (going from bottom to top in the figure) is lowest for H8s with high MIP, indicating evolutionary conservation of this feature of H8 once a high MIP has been acquired (Fig. 7F, top). Next, we assessed the distribution of MIP values for individual species across evolution (Fig. 7F, histograms to the right). Intriguingly, in Ecdysozoa, the distribution of MIP values (histograms to the right) displays a single peak overlaying with values obtained from randomly generated sequences (indicated by the dashed line). However, as seen from the evolution of histograms going from bottom to top, the fraction of receptors with high MIP of H8 (>0.3) gradually increases in higher organisms indicating functional selection of MIP (Fig. 7F). This functional selection and refinement is evident from the multimodal distribution of H8 MIP values across human GPCRs, significantly different from a normal distribution (Fig. 4H, $P < 0.0001$, Shapiro-Wilk test). Together, these findings suggest both evolutionary selection and refinement as well as functional conservation of the MIP value of H8 in GPCRs.

## DISCUSSION

Here, we show that AHs facilitate TMP association with areas of high membrane curvature similar to what has been demonstrated for cytosolic proteins. For TMPs, this association accelerates their constitutive trafficking in a manner that correlates with the MIP of their AHs. While this paper focused on endocytosis, we show evidence that this mechanism, due to the basic biophysical principle, is likely to apply to trafficking events throughout the endomembrane system involving highly curved membrane topologies and serve as a key determinant for steady-state distribution of GPCRs together with adaptor-based sorting and trafficking. We term this mechanism ToTAM, and, combining the association with the COP machinery in the biosynthetic pathway and the association with the early part of the clathrin machinery at the plasma membrane, we envision that the mechanism localizes TMPs specifically to high curvature membranes undergoing initial budding where they will facilitate vesiculation and scission. Predictably, this mechanism increases steady-state association with vesicular and highly curved membranes at the expense of relatively flat membranes such as most of the plasma membrane and rough ER as evidenced by the BioID experiments and directs endocytic cargo toward recycling structures at the expense

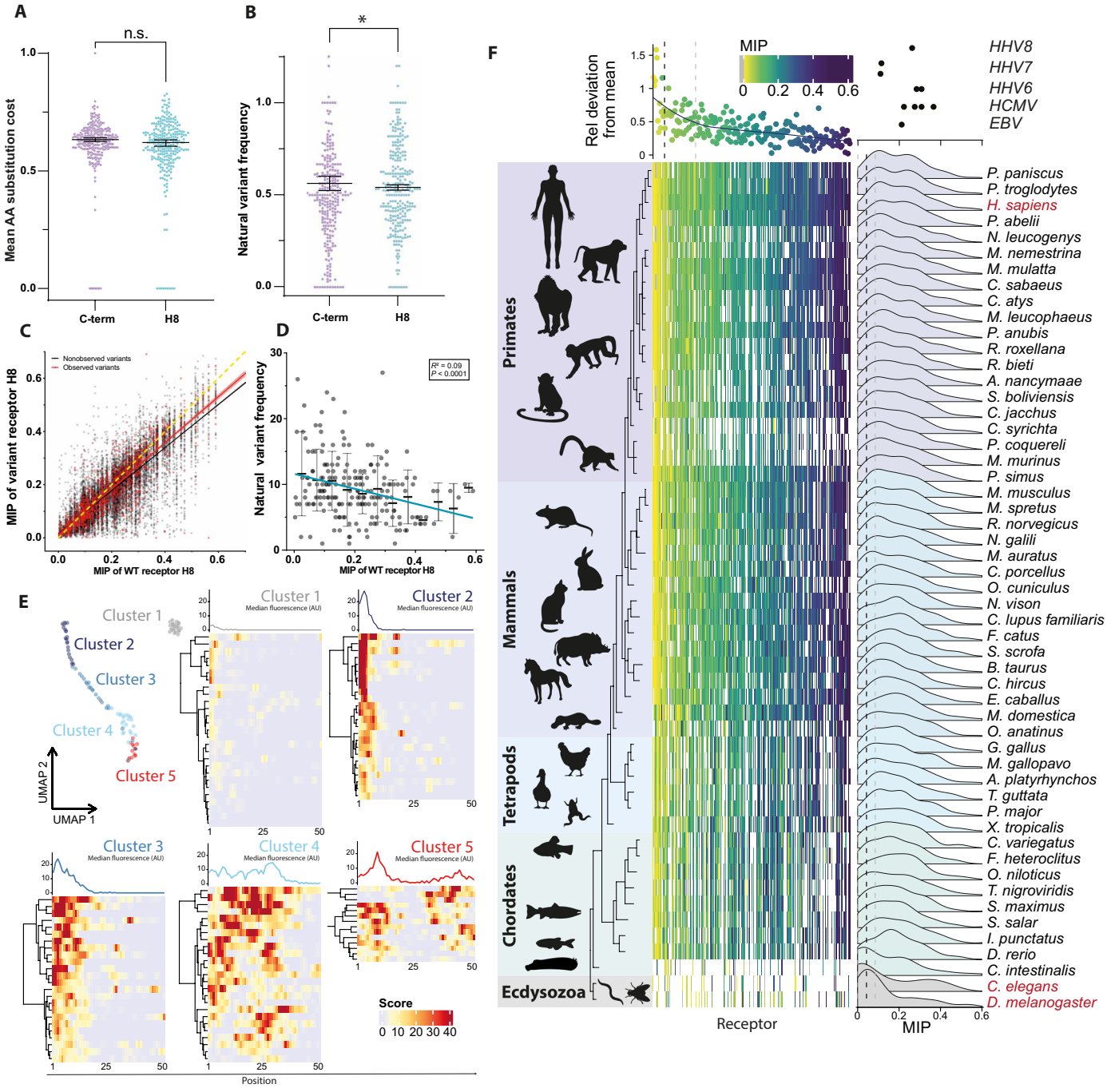


**Fig. 7. Functional conservation and evolutionary refinement of MIP of H8 in GPCRs.** (**A**) Normalized BLOSUM62 (*60*) substitution cost of natural variants mapped to full C terminus versus H8. AA, amino acid. (**B**) Frequency of natural variants (UK Biobank) (*61*) in the full C terminus (C-term) versus H8 of human GPCRs of clusters 2 to 6. [(A) and (B)] Wilcoxon nonparametric statistical test. Asterisks indicate *P* value of $< 0.05$ and n.s. *P* value of $> 0.05$. (**C**) Scatter plot of MIP values of all identified nonsynonymous natural variants (red dots) identified in the UK Biobank (*61*) and nonidentified possible nonsynonymous substitutions (black dots) as a function of the wildtype receptors MIP. Linear regression analysis of observed natural variants with a slope of $0.87 \pm 0.01$ is closer to full conservation (indicated by dashed yellow line, slope of 1) than for nonobserved $0.81 \pm 0.004$ (all other possible variants). (**D**) Scatter plot showing frequency of nonsynonymous natural variants of individual GPCRs as a function of MIP (each receptor represented by a dot), with a negative linear correlation indicating lowered variant frequency for receptors with high MIP (cyan, $R^2 = 0.089$, $P < 0.0001$). Lines indicate average frequency of binned MIP intervals $\pm$ SD. (**E**) UMAP-based clustering of combined *D. melanogaster*, *C. elegans*, and *S. cerevisiae* GPCR C termini based on position and strength of liposome binding motifs. Heatmaps of individual GPCR C-terminal liposome binding profiles within the five clusters and profile plots of their median fluorescence (top) (see fig. S30 for the list of individual receptors and species). (**F**) Evolutionary tree of GPCRs displaying MIP of H8 sequences identified in human receptors and aligned across species (left). The ratio of variance versus mean of all MIP decreases with increasing MIP (top, left). Top, right: MIP values for viral GPCRs (table S2). Bottom, right: Density distribution of MIP values for individual species shift to the right during evolution. $^*P < 0.05$, $^{**}P < 0.01$, $^{***}P < 0.001$, and $^{****}P < 0.0001$. AU, arbitrary units.

of the lysosomal pathway. Much is yet to be understood in terms of how ToTAM targets TMPs to vesicular versus tubular pathways, as well as how it balances anterograde and retrograde trafficking in the synthetic pathway, and how it might be involved in partitioning TMPs to, e.g., mitochondria and peroxisomes.

Mechanistically, endocytosis by ToTAM is characterized by fast, cooperative cargo recruitment into small, spherical, high-density carriers, and, thus, ToTAM displays elements of both MCS and facilitation of the cargo/carrier complex formation. ToTAM increases endocytosis of the TfR in trans, implying an active impact on endocytic processes.

During this process, partial biochemical association with CME was observed; however, actual CLC accumulation before scission was low and increasingly asynchronous with higher MIP of the AHs.

Together, our data suggest that ToTAM might hijack nucleation involving CLC and EPS15 to shortcut classical CME in an autonomous fashion that is complementary to the established adaptor-based endocytic machinery. The increased transferrin uptake in trans, thus, could result from ToTAM-mediated stabilization of EPS15-nucleated structures accumulating TfRs at early endocytic sites. Alternatively, ToTAM might actively facilitate dynamin independent membrane scission as suggested by the dominant negative experiments, highlighting partial dependence on EPS15, but not dynamin, or a combination of both.

The impact of high MIP H8 specifically on constitutive, and not agonist-induced, internalization of full-length GPCRs was causally demonstrated by experiments with chimeric receptors, making them unable to interact with, e.g., PDZ-domain proteins. Also, this experiment used overexpression in a simple cell (HEK293), and, consequently, several layers of regulation are likely to overlay ToTAM for endogenous receptors in complex tissues. Using large-scale liposome-binding data to exclude GPCRs with C termini that did not display membrane-binding (cluster 1) or complex membrane binding (cluster 6) enabled us to correlate H8 MIP with full-length constitutive internalization across all human GPCRs. For the clusters that show simple membrane binding in a region corresponding to helix 8 (clusters 2 to 5), the term synaptic transmission was the most enriched GO term. This aligns with receptors for biogenic amines (including receptors for serotonin, acetylcholine, noradrenaline/adrenaline, dopamine, and histamine) as well as the opioid and trace amine–activated receptors almost without exception showing robust membrane binding. Both in the peripheral and central nervous system, these receptors are generally involved in faster and more dynamic signaling than seen for, e.g., circulating peptide hormones evidenced, e.g., by receptors in group B1. We speculate that the capacity to undergo high constitutive internalization provides a basis for efficient local and temporal control of signaling in concert with regulatory proteins or that the fast transmission may require efficient receptor recycling to sustain signaling capacity. We also note that receptors prone to development of tolerance upon therapeutic treatment including μ-opioid, cannabinoid 1, serotonin 5-HT2A, histamine H1, dopamine D2, α1 and 2-adrenergic, and β2-adrenergic receptor all belong within this group. This feature has previously been linked to β-arrestin recruitment, but, because MIP and β-arrestin did not show any correlation here, it will be interesting to assess whether the high MIP of their H8 might explain this feature independently of β-arrestin. Receptors activated by lipid molecules including free fatty acids, sphingosine, and cannabinoids also demonstrate strong membrane binding, predicting significant localization to intracellular compartment. Because lipid transmitters are partly membrane permeable, the high constitutive internalization propensity might underlie their capacity for signaling from endosomal compartments as seen for, e.g., the CB1 receptor. Note that CB1, which has a membrane binding helix 9 in addition to H8 (*42*, *43*), belongs to cluster 6, which shows complex membrane binding. Consequently, the MIP that we report for the H8 region alone underestimates the total MIP for the C terminus of GPCRs belonging to this cluster. Last, MAS-related and chemokine receptors show high H8 membrane binding. It will be interesting to elucidate the functional implication of the predicted high constitutive turnover in relation to ligand scavenging for these receptors. Conversely, and perhaps more unexpectedly, many of the GPCRs did not show appreciable membrane binding of their C-terminal regions (cluster 1). These include not only many class B2 and C receptors but also evolutionary-related subclusters within class A such as the opsins and the formyl peptide receptors, melanocortin receptors, as well as several individual orphan receptors. Notably, this cluster is enriched in photoreceptor discs and exosomes, suggesting that a H8 with high MIP is likely to exclude localization to these structures. Exosomes are topologically poorly compatible with membrane insertion of H8, and ToTAM is likely to sort such receptors toward recycling rather than to multivesicular bodies. In addition, because photoreceptor discs are formed from modified primary cilium, these are also topologically poorly compatible with membrane insertion of H8 and receptors localized to primary cilia displayed H8 MIP values significantly below average. In the absence of ToTAM, cilia localization, including localization of opsins to the photoreceptor discs, is highly abundant in short linear localization motifs (*44*), which are not restricted by membrane topology.

Another recently described membrane-associated function of H8 is its role in conferring mechanosensitivity to GPCRs (*45*). Several of these receptors include a H8 with high MIP, including $H_1$, $AT_1$, and $S1P_1$. A putative interplay between mechanosensation and high constitutive internalization due to MCS might reflect two aspects of the same biophysical principle, and functional implications of these might unveil themselves perhaps in the context of the cardiovascular system. Moreover, GPCRs implicated in viral entry, as well as virally expressed GPCRs displaying high constitutive internalization, all except that mGluR2 shows high MIP (*46*), potentially advocating an alternative type of molecular target for antiviral therapy. Last, the simple molecular nature of ToTAM is compatible with an early evolutionary origin, dating back before the yeast GPCRs characterized here, conceivably even before adaptor-based trafficking. Ultimately, functional studies will be needed to settle the evolutionary relation between these two complementary trafficking mechanisms.

## MATERIALS AND METHODS

### Molecular biology

Coding sequences for the AHs (outlined below) were synthesized and cloned in frame into a pcDNA3 Flag Tac construct using Hind III and Xba I sites. The amino acid sequence of Tac is largely equivalent to the interleukin-2 receptor subunit α, with a FLAG-tag (DYKDDDDK) sequence inserted downstream of the signal peptide sequence and a trailing QASS sequence at the C terminus (see fig. S4). The C-terminal serine is replaced with the following inserts containing putative helical sequences listed in table S1. Full-length angiotensin receptor (ATR) was a gift from T. W. Schwartz (Metabolic Receptology, University of Copenhagen), and b2AR was distributed by

M. von Zastrow (Department of Psychiatry, University of California, San Francisco, USA). Di-glutamate mutations were introduced following Quick Change method (Stratagene, La Jolla, CA, USA).

SEP constructs were produced using polymerase chain reaction amplification and subsequently inserted by restriction enzyme cloning. Chimeric constructs were produced using QuickChange method (Stratagene, La Jolla, CA, USA). PRESTO-Tango library was acquired from Addgene (Kit no. 1000000068). FLAG-TacAH-BioID2 constructs were prepared using Sequence and Ligation Independent Cloning (SLIC) method (*47*), amplifying the coding region of BioID2 (*25*) (Addgene, plasmid no. 74224), and inserting it downstream of FLAG-TacAH with a five–amino acid linker sequence (AAGGS). All constructs were verified by DNA sequencing.

### Cell cultures

Human embryonic cells (HEK293), BSC-1 cells, and HeLa cells were cultivated in growth medium [Dulbecco's modified Eagle's medium 1965 (DMEM) supplemented with 10% fetal bovine serum (FBS) and 1% penicillin/streptomycin] and maintained at 37°C and 5% $CO_2$ levels. Cells were subcultured every 3 to 4 days for maintenance to a maximum passage of 35 and never allowed to reach a confluency above 95%.

### Transient transfection for internalization assays

A day before transfection, cells were seeded on poly-L-ornithine–treated coverslips in triphenylphosphine (TPP) polystyrene six-well plates (Sigma-Aldrich) at a density of $3.5 \times 10^5$ cells per well, unless otherwise stated. Transfection was performed using Lipofectamine 2000 and Opti-MEM (Thermo Fisher Scientific). The manufacturer's protocol was followed with a 3:1 lipofectamine-to-DNA ratio. A total of 0.5 to 1.5 μg per well was used, and cells were incubated with transfection mix in Opti-MEM for 5 hours. Opti-MEM was replaced with growth medium, and cells were used for experiments 48 hours after transfection.

### Antibody conjugation

Primary anti-FLAG M1 antibodies used for feeding assay were fluorescently labeled by *N*-hydroxysuccinimide (NHS)–ester fluorophore conjugation. A 90-μl antibody solution (1 mg/ml) was added to 10 μl of $NaHCO_3$ (1 M) and 5 μl of NHS-ester fluorophore (Alexa Fluor 488 or Alexa Fluor 647) (1 mg/ml). The mixture was incubated for 1 hour at 25°C, and antibodies were isolated using illustra NAP-5 columns (GE Healthcare Life Sciences), resulting in an average labeling rate of four and eight dye molecules per antibody for 488 and 647 respectively, as measured on a Thermo Fisher Scientific NanoDrop 2000c.

### Antibody feeding assay for confocal imaging

On day of experiment, cells were incubated with primary anti-FLAG M1 antibody (1 μg/ml in Opti-MEM, for 1 hour at 4°C). Cells were then exposed to prewarmed (37°C) growth medium containing 25 μM monensin (Sigma-Aldrich) and kept at 37°C for 30 min. Cells were fixed in a 4% paraformaldehyde (PFA) solution in phosphate-buffered saline (PBS) for 10 min and subsequently washed with PBS. Next, cells were passivated using blocking buffer [5% goat serum (GS) in PBS] and incubated for 20 min at 25°C. Surface-bound M1 antibody was labeled using Alexa Fluor 488–conjugated goat anti-mouse secondary antibody (1:200 in 5% GS, 1 hour, 25°C). Cells were fixed again in 4% PFA in PBS for 10 min at 4°C, washed in PBS, and permeabilized with 0.2% saponin and 5% GS in PBS (30 min at 25°C). Next, cells were incubated with Alexa Fluor 568–conjugated secondary goat anti-mouse antibody (1:500, 5% GS, 30 min 25°C). Last, cells were washed three times with PBS, and coverslips were mounted using 4′,6-diamidino-2-phenylindole Fluoromount-G (SouthernBiotech).

Selective interference of actin polymerization, macropinocytosis, and dynamin constriction was performed by addition of 200 nM latrunculin A (Thermo Fisher Scientific), 1 μM EIPA, and 10 μM Dyngo-4A (Abcam) during 30-min internalization period, respectively.

Cells were imaged as *z*-stacks with increments of ~700 nm using either a Zeiss Confocor 2 confocal microscope (LSM 510) or Zeiss Axoimager M2 confocal microscope (LSM700) with a Plan-Apochromat oil immersion objective with a ×63 magnification and numerical aperture (NA) of 1.4 (Carl Zeiss, Oberkochen, Germany). Fixed samples were imaged in frames of 1024 by 1024 resolution, 8 bits, in line-scanning mode with two times averaging. Alexa Fluor 568 dye was excited using 543/555-nm laser light from a helium-neon (HeNe) laser or diode source, and emitted fluorescent light was filtered using a 585-nm long-pass filter or none. Alexa Fluor 488 dye was excited using a 488-nm laser line from an argon-krypton laser or diode, and the emitted light was filtered using a long-pass 505- to 530-nm barrier filter or none. Channels were imaged separately. Image processing was performed using Fiji (National Institutes of Health) (*48*). Region of interests (ROIs) were selected to accommodate entire cells throughout the stack, as inspected through green channel only (up to a maximum of four ROIs per image). The threshold was set to exclude background noise and kept constant throughout independent experiments, and all images were masked. Intensities were quantified independently for each stack in each channel and saved as comma separated files. A MATLAB script was generated to automatically import data and calculate overall intensity ratios for each cell. Individual ratios for each cell were $\log_{10}$ transformed before averaging within each construct and normalization to Tac. Averages and SEM were determined within each experiment on basis of a minimum of 10 individual cells. Linear regression analysis was performed using Prism (GraphPad Software Inc.). All ROIs were saved for later inspection.

### Antibody feeding assay for flow cytometry

Cells were seeded in TPP polystyrene six-well plates (Sigma-Aldrich), transfected as described above, and kept in plates until experiment. On day of experiment, cells were incubated with Alexa Fluor 647–conjugated primary anti-FLAG M1 antibody (1 μg/ml, 1 hour at 4°C). Cells were then exposed to prewarmed (37°C) growth medium containing 25 μM monensin and kept at 37°C for 30 min. For experiments with chimeric constructs, internalization medium additionally included 10 μM isoproterenol and 10 μM angiotensin 2 for β2AR and AT1R, respectively. Cell surfaces were stripped for antibody by addition of cold strip buffer (0.5 M NaCl and 0.2 acetic acid) and incubation for 5 min followed by a wash in PBS and cold labeling with Alexa Fluor 488–conjugated primary anti-FLAG M1 antibody (1 μg/ml, 1 hour at 4°C). Cells were collected using cold PBS and transferred to Eppendorf tubes, spun down at 2000*g* for 10 min, and resuspended in 4% PFA before flow cytometry acquisition.

Samples were run on a FACSCalibur flow cytometer (BD Biosciences) and analyzed with FlowLogic software (Inivai Technologies). Briefly, empty pcDNA3-transfected cells without fluorophores were used to gate cells from debris through a combination of SSC-H and

FCS-H signals (fig. S3). Unspecific fluorescence gating was set to include a maximum of 1% of events from untransfected cells, otherwise treated identical to samples. Only events corresponding to gated cells with specific fluorescence signal were used for further analysis. Alexa Fluor 488 was excited using a 488-nm argon laser, and the emitted fluorescence was filtered through a 530/30 band pass (BP) filter and collected by a photomultiplier tube (PMT) (FL-1). Alexa Fluor 647 was excited using a 635-nm diode laser, and the emitted fluorescence was filtered through a 661/16 BP filter and collected by a PMT (FL-4). Extracted intensities in FL-1 and FL-4 channels were used for quantification. Briefly, a 2D dot plot of the intensities of surface bound (FL-1) and internalized fluorophores (FL-4) for each investigated cell of each construct was analyzed using a python-based random sample consensus algorithm from scikit-learn (*49*), giving an outlier optimized linear regression slope with minimized influence of outliers. The resulting slopes were normalized to the reference construct Tac, yielding relative internalization.

The preparations for timeline experiments were done by incubating transfected cells with Alexa Fluor 647–conjugated primary anti-FLAG M1 antibody (1 μg/ml, 1 hour at 4°C) and then incubating at 37°C for indicated time periods with prewarmed (37°C) growth medium containing 25 μM monensin. Surface-bound antibodies were stripped by 5-min incubation with cold strip buffer (0.5 M NaCl and 0.2 acetic acid). Cells were fixed and run on FACSCalibur flow cytometer for acquisition. Internalization was quantified as mean Alexa Fluor 647 signal subtracted by the mean signal obtained from samples at time point 0 in percentage of the same signal obtained for samples that were only cold labeled.

### Transferrin uptake by flow cytometry

Cells were seeded in TPP polystyrene six-well plates (Sigma-Aldrich), transfected as described above, and kept in plates until experiment. On day of experiment, cells were incubated with Alexa Fluor 488–conjugated primary anti-FLAG M1 antibody (1 μg/ml, 1 hour at 4°C) and Alexa Fluor 647–conjugated transferrin (25 μg/ml) (Thermo Fisher Scientific). Cells were then exposed to prewarmed (37°C) growth medium containing 25 μM monensin and kept at 37°C for 12 min. All cells were collected in cold PBS and transferred to Eppendorf tubes, spun down at 2000*g* for 10 min, and resuspended in 4% PFA before acquisition in flow cytometer. Samples were run on a FACSCalibur flow cytometer (BD Biosciences) and analyzed with FlowLogic software (Inivai Technologies) similar to what was described for antibody feeding assays.

### Live-cell imaging on ppH TIRF setup for endocytosis

Live-cell imaging was performed at 37°C. Cells were perfused with Hepes-buffered saline (HBS) solution (135 mM NaCl, 5 mM KCl, 0.4 mM $MgCl_2$, 1.8 mM $CaCl_2$, 20 mM Hepes, and 1 mM D-glucose, adjusted to pH 7.4 and 300 to 315 mosmol/liter). For the ppH protocol, a theta pipette ~100-μm tip size achieved using a vertical Narishige puller (World Precision Instruments) was placed in proximity of the recorded cell. One outlet contained HBS (pH 7.4; see previous paragraph for recipe) and the other contained a solution where Hepes was replaced with MES (MES-buffered saline solution) and buffered at pH 5.5. Solution flow was alternated every 2 s using electrovalves (Lee Company) switching in synchrony with image acquisition. TIRF imaging was performed on an inverted microscope (IX71; Olympus) equipped with an Apochromat N oil 60× objective (NA of 1.49), a 1.6× magnifying lens, and an electron-multiplying charge-coupled device (EM-CCD) camera (QuantEM:512SC; Roper Scientific). Samples were illuminated by a 473-nm laser (Cobolt) for SEP imaging, as well as by a coaligned 561-nm laser for red fluorescent protein (FP) imaging. Emitted fluorescence was filtered using the following filters (Chroma Technology Corp.): 620/60 m for mCherry imaging and 525/50 m for SEP/green fluorescent protein fluorescence. Simultaneous dual-color imaging was achieved using a DualView beam splitter (Roper Scientific) and dual cameras. To correct for *x*/*y* distortions between the two channels, images of fluorescently labeled beads (Tetraspeck, 0.2 μm; Invitrogen) were taken before each experiment and used to align the two channels (see Quantification of fluorescence intensities). The camera was controlled by MetaVue7.1 (Roper Scientific).

### Detection and quantification of endocytic events in ppH-TIRF

Detection and subsequent quantification of fluorescent protein assemblies was done as previously described (*35*). Briefly, spots were subjected to segmentation on the basis of wavelet transform multidimensional image analysis. The objects detected were then tracked using a simulated annealing algorithm to identify endocytic events. The output of this tracking was a series of coordinates corresponding to the center of mass of the objects, with unique identifiers (event numbers). All the observed fluorescent assemblies in the TfR5.5 movies were screened to identify genuine endocytic events using routines programmed in MATLAB 7.4 (MathWorks). To qualify as bona fide events, each candidate event required a TfR5.5 vesicle (i) that persisted for at least three frames (i.e., 8 s) following appearance; (ii) that appeared at least 20 frames after the start of the movie, or 20 frames before its end, to ensure quantification of signals for 80 s before and after the vesicle's appearance; (iii) that appeared and remained at more than seven pixels (0.7 μm) from the edge of the image to ensure proper quantification (see below); (iv) that appeared de novo and was not produced by the fusion of two objects or the dissociation of an object into two; (v) that overlapped, on appearance, with a preexisting cluster detected in the segmented TfR7.4 movie; (vi) whose fluorescence was bigger than a defined signal-to-noise ratio (SNR) of 5, wherein SNR = $(F_0 - \mathrm{av})/\mathrm{SD}$, where $F_0$ is the fluorescence at time 0, and av and SD are the average fluorescence and standard deviation, respectively, in the five frames before vesicle appearance; and (vii) that was close to maximal fluorescence at the time of appearance. We calculated the slope of the fluorescence change in the first three frames of vesicle appearance and discarded the events where this slope was greater than 0.1, which corresponds to a 10% increase in fluorescence.

### Characterization of trace profiles from ppH-TIRF

While the spatial and temporal extension of the fluorescent traces in the TfR5.5 channel is defined directly by the formation and acidification of single vesicle carriers, the fluorescent traces describing clusters in TfR7.4, CLC5.5, and CLC7.4 can encompass and span several events. The resultant profile characteristics, therefore, contain important information of the underlying mechanistic of each construct. Hence, we initially assessed the CLC profiles and TfR7.4 profiles connected to each TfR5.5 event by normalizing each of the traces individually, smoothening the traces by a loess model to remove noise, and ultimately generating collected raster plots for each construct (fig. S13 and Figs. 2J and 3A).

In the case of TfR7.4 profiles, we used these collections to estimate the overall recruitment rates and collaborative nature of the clusters comparatively by performing logistic fitting of the profiles just before scission ($t = [-20{:}0]$) to an adapted version of the Langmuir-Hill equation: $\theta = 1/[1 + (T50/t)]^H$, where θ is the fraction of total cluster size estimated at the time of scission, $t$ is the time from −20 to time of scission, $T50$ is the time where cluster is grown to half size, and $H$ is the Hills coefficient. These fits allowed to extract the Hills coefficient as a measure for the collaborative recruitment of constructs during accumulation.

As the collected CLC profiles (CLC5.5/7.4 interleaved) contained information of the overall activity surrounding the individual events (figs. S13 and S14), we performed a PCA on all the normalized traces pooled together to evaluate the principal components giving rise to the observed profiles. Together, the first four principal components contained 63.9% of the total variance and were used to sort and the individual raster plots and evaluate the governing mechanics pertaining to each construct

### High-frequency live-cell imaging for exocytosis studies

Live-cell imaging was performed at 37°C. Transfected BSC-1 cells were grown in LabTek2 chambers and imaged using a Nikon Eclipse Ti-E epifluorescence/TIRF microscope (Nikon) equipped with a 405-nm laser (coherent) and a triple line 405/488/561 beam splitter. Cells were kept in growth medium before imaging, and medium was substituted for temperature-equilibrated PBS buffer to reduce background fluorescence during imaging.

The emission signal from pHluorin constructs and CLC-mCherry was split by a 509-nm beam splitter (AHF analysentechnik AG), the pHluorin signal was filtered using a 466/40-nm BP filter, and the CLC-mCherry signal by a long pass (LP) filter. Light was directed to a dual-view adaptor collected by two EM-CCD cameras (iXon3 897, Andor).

### SPOT assay

Peptide arrays were prepared as described in (*50*) with sequences identical to the Flag-TacAH-construct inserts. We developed and optimized a protocol for liposome binding (*51*). In brief, plates were coated with 5% bovine serum albumin (BSA) before binding, washed, and exposed to a dilution of bovine brain liposomes (0.01 mg/ml) containing 0.5% biotin. Liposomes were made by dissolving Folch bovine brain lipids in chloroform together with 0.5% dioleoylphosphatidylethanolamine (DOPE)-biotin, evaporating samples with $N_2$, and rehydrating in buffer to a final concentration of 1 mg/ml. After eight freeze-thaw cycles, the liposomes were sonicated briefly at low intensity, subjected to another freeze-thaw cycle, and stored at 4°C until use. Storage time was always kept below 36 hours. The arrays were incubated with liposomes for 30 min at 25°C, washed three times in PBS, and exposed to 5 ml of an avidin–horseradish peroxidase (HRP) solution (0.01 mg/ml) to cover the entire array. Arrays were allowed to equilibrate for 30 min at room temperature, washed three times in PBS, and moved to an Alpha Innotech MultiImage Light Cabinet, where it was covered with electrochemiluminescence substrate and imaged. Total intensities were quantified with ImageJ.

### Data retrieval of membrane proximal C-terminal regions in GPCRs

We extracted the complete set of *Homo sapiens* (taxid: 9606) gene products from the Universal Protein Resource Knowledgebase (UniProtKB) Swiss-Prot database with the GO annotation "part of integral component of membrane" (GO:0016021) and "G protein–coupled receptor activity" (GO:0004930) from the EBI GO Annotation database (GOA) (www.ebi.ac.uk/GOA, 2020-08-17). This resulted in a dataset containing 807 distinct gene products. Gene products annotated with "olfactory receptor activity" (GO:0004984) were removed resulting in 410 gene products. The resulting gene products were exported as a Gene Product Association Data file. The UniProtKB accession numbers were used to extract their respective topological data from the UniProtKB (www.uniprot.org/). The following extraction, sorting, and analysis of data were performed using the programming language R (version 4.0.2) in RStudio (version 1.4.1013). Sequences were analyzed for annotated regions of secondary structure and intermembrane regions. The identified regions were removed from the sequences, and only the regions residing in proximity to transmembrane domains were kept in the dataset. We added all C termini from *S. Cerevisiae*, *C. elegans*, and *D. Melanogaster* GPCRs to the dataset (140 GPCRs as obtained from the GO resource), enabling an evolutionary conservation analysis. The resulting sequences were split into 16-nucleotide oligomer cassettes overlapping by 14 amino acids (two–amino acid resolution), which resulted in 15,198 unique peptides.

### High-density peptide array synthesis and scanning

Synthesis was performed by Schafer-N ApS, Lersö Park Allé 42, DK-2100 Copenhagen, as described by Schafer-Nielsen and coworkers (*52*). All unique in silico–extracted 14–amino acid overlapping 16-nucleotide oligomer GPCR-specific peptides were randomly split into six evenly sized groups and synthesized onto six equally sized sectors on the array. Each peptide was synthesized in a 20 μm–by–20 μm field, separated from other fields by 10 μm from all sides. As a positive control for liposome binding Hecate (LKKALKKLKKALKKAL) was synthesized in the 17 peptide fields encompassing each of the corners of the six sectors on the array. All peptides were synthesized onto the array with a short C-terminal linker KSGG. A total of 510 negative controls, fields not containing peptides, were spread randomly across the array. The array was blocked using 5% BSA in PBS with 2 mM dithiothreitol (DTT) for 1 hour on a shaker at 120 rpm and then washed three times in PBS for 20 min. The array was incubated with DiD-labeled liposomes diluted 1:100 in PBS (pH 7.4) for 1 hour at room temperature. Subsequently, the array was washed twice in PBS for 5 min and an additional time for 20 min. Following 30-s washes (3×) with 0.1% Tween 20 in PBS, the array was dried by centrifugation (30 s) and scanned at 1-μm resolution with an InnoScan 900 laser-scanner (INNOPSYS) with an excitation wavelength of 635 nm and gain setting of 6 with the high-power setting to obtain the image used for this analysis.

### Conditional GO term enrichment analysis

All nonolfactory human GPCRs represented were selected from the array data by exclusion of olfactory GPCRs annotated with GO term GO:0004984 (olfactory receptor activity). GO terms were imported via pantherdb.org using rbioapi package in R (date time: 23 September 2024, 18:08). Conditional enrichment was run for each cluster using the topGO package in R algorithm = "weight01," test = "fisher." The Resnik GO term similarity was calculated in each cluster using the simplifyEnrichment package in R with the background population set to GPCRs manually. Similarity matrix was clustered using a binary cut or *k*-means. Keyword enrichment was performed for

each cluster (or clusters 2 to 5 combined) (Fisher test versus GPCR GO terms). GO term similarity matrix was plotted with significantly enriched cluster associated keywords for clusters with $n > 4$ terms

### Liposome preparation

Liposomes were generated using a heterogeneous lipid extract from bovine brain (type I, Folch fraction I, Sigma-Aldrich). Lipid extract (0.5 mg) was dissolved in 1 ml of chloroform, before addition of 2% DiD (Invitrogen) (w/w). Lipids were dried with $N_2$-gas while rotating, creating a thin lipid film, followed by vacuum dehydration for 12 hours to remove residual chloroform. Lipids were rehydrated in a sterile filtered PBS (pH 7.4) to a final concentration of 1 mg/ml. The rehydrated lipids were put through eight freeze-thaw cycles using liquid nitrogen and a 40° to 50°C water bath. The liposomes were extruded through a 19-mm polycarbonate Whatman Nuclepore Track-Etched membrane with a pore size of 1 μm using a LiposoFast liposome extruder (Avestin). The liposomes were extruded 18 times before being diluted 1:1000 in sterile PBS.

### 3D-dSTORM—Sample preparation

BSC-1 cells were seeded on coverslips in TPP polystyrene six-well plates (Sigma-Aldrich), transfected as described above, and kept in plates until experiment. On day of experiment, cells were fixed using a 4% PFA solution (10 min at 4°C), washed in PBS (3×), and passivated using blocking buffer (1% BSA and 5% GS solution in PBS) for 20 min before incubation with anti-FLAG M1 antibody (1 μg/ml in 1% BSA and 5% GS solution for 1 hour at 25°C, Thermo Fisher Scientific). Cells were washed in PBS (3×), fixed in a 4% PFA solution (10 min at 4°C), washed again (3×), before being passivated for 20 min, and incubated with secondary Alexa Fluor 647–conjugated anti-mouse antibody (1 μg/ml in 1% BSA and 5% GS solution for 45 min at 25°C, Thermo Fisher Scientific). Last, cells were washed in PBS (3×), fixed using 4% PFA solution (10 min at 4°C), and washed once in PBS containing 20 mM glycine and 15 mM ammonium chloride to quench free aldehydes, followed by wash in PBS (2×). The fixed samples were then transferred to a quick release imaging chamber and imaged in a buffer containing glucose oxidase (560 g/ml), catalase (34 g/ml), 2 mM cyclooctatetraene, 1% 2-mercaptoethanol, 50 mM tris-HCl (pH 8), 10 mM NaCl, and 10% glucose in water.

### 3D-dSTORM—Optical setup and image acquisition

Single-molecule localization imaging was performed on a Zeiss Elyra PS.1 inverse microscope. Samples were illuminated using 405- and 642-nm high repetition rate (HR) diode lasers with maximum power levels of 5 and 150 mW, respectively. The 642-nm laser was used at maximum power, while the 405-nm laser was used to reactivate Alexa Fluor 647 fluorophores, and power was incrementally increased by 0.1 percentage points. Light was collected in a Plan-Apochromat 63× oil objective with an effective NA of 1.4. Emitted fluorescence was collected in the same objective and further magnified using a 1.6× tube lens. Emission was filtered using a 655 LP filter and captured by a cooled EM-CCD camera (Andor, iXon DU897) at 55.6 Hz. For 3D localizations, we applied a double-phase ramp module (Zeiss) for phase ramp imaging localization microscopy. 3D information was acquired from the *z*-position–dependent rotational angle of the two lobes emanating from each fluorophore given the double-phase ramp module (*53*). All 3D-single-molecule localization microscopy (SMLM) experiments were conducted in highly inclined and laminated optical sheet illumination mode. A total of 30,000 frames were recorded for each video.

### 3D-dSTORM—Analysis

Localizations were fit using the spliner implementation of the 3D-DAOSTORM code package (*54*). Calibrations were made using 100-nm fluorescent TetraSpeck beads. The beads were attached to a coverslip by initial addition of 50 μl of 1 M $MgCl_2$ followed by deposition of 0.9 μl of beads diluted in 500 μl of water. Clustering of the data was performed using a DBSCAN algorithm, identifying clusters within a 60-nm radius of each localization with at least 15 qualifying neighbors. Given the reduced axial resolution compared to lateral resolution, we set the weighting of axial position versus lateral to 0.5. Several parameters were extracted for each cluster, including maximum size in the *x*, *y*, and *z* directions, radius of gyration, and density of localizations.

### Transient transfection for BioID2-MS assay

A day before transfection, low-passage (below 15) HEK293 cells were seeded in tissue culture (TC)-treated T-175 culture flasks (Sigma-Aldrich) at a density of $5 \times 10^6$ cells per flask. Transfection was performed using Lipofectamin 2000 and Opti-MEM (Thermo Fisher Scientific). The manufacturer's protocol was followed with a 3:1 Lipofectamin to DNA ratio. A total of 20 μg per well was used, and cells were incubated with transfection mix in Opti-MEM for 5 hours. Opti-MEM was replaced with biotin supplemented growth medium [50:50 F10 and DMEM (Thermo Fisher Scientific)], and cells were used for experiments 24 hours after transfection.

### Proximity biotinylation pull-down assay

On the day of experiment, biotin-containing growth medium was decanted, and cells were washed twice with PBS. The second wash was performed with ice-cold PBS (4°C)–containing complete protease inhibitor cocktail tablets and phosphatase inhibitor cocktail 3 (Sigma-Aldrich). Cells were subsequently kept at 4°C for the rest of the purification steps. Cells were collected and spun down at 300*g* for 5 min. Supernatant was decanted, and the pellets were snap frozen in liquid nitrogen. Pellets were resuspended in 1 ml of ice-cold radioimmunoprecipitation assay (RIPA) lysis buffer (150 mM NaCl, 0.1% SDS, 0.2% NP-40, and protease inhibitor in 50 mM tris-HCl at pH 7.5) and homogenized using a handheld homogenizer gun. The homogenate was incubated for 2 hours with end-over-end rotation. The lysates were centrifuged at 13,000*g* for 15 min. The resulting supernatant was transferred to fresh tubes and incubated with prewashed (in RIPA buffer) magnetic streptavidin-coated Dynabeads slurry (50 μl per sample) for 1 hour with end-over-end rotation. Liquid was removed from Dynabeads using a magnetic DynaMag rack. Subsequently, beads were washed using a regimen of 2× low-salt [100 mM KCl and 0.1% Triton X-100 (TX-100) in 20 mM tris-HCl at pH 7.5], 2× high-salt (500 mM KCl and 0.1% TX-100 in 20 mM tris-HCl at pH 7.5), and 2× low-salt and 1× moderate-salt buffer (150 mM KCl and 0.1% TX-100 in 20 mM tris-HCl at pH 7.5) before a wash in PBS; transferred to fresh tubes; and lastly washed in PBS. On-bead digestion using trypsin and subsequent LC-MS/MS analysis were performed by the Proteomics Research Infrastructure facility of the Faculty of Health and Medical Sciences at the University of Copenhagen.

### Analysis and data presentation

Raw LC-MS/MS data files were directly loaded as input in MaxQuant software (version 1.6.15.0) (*55*). The Andromeda search analyzed the

runs against the Human reference proteome UP000005640 (downloaded from UniProtKB database in March 2021), and a 1% false discovery rate (FDR) peptide and protein cutoff were used. We specified carbamidomethylation on cysteines as fixed modification, and oxidation (M) and N-term acetylation were set as variable modifications. Trypsin was selected as proteolytic enzyme, allowing a maximum of two missed cleavage sites. Results were filtered for a minimal peptide length of seven amino acids. We enabled match-between runs with a matching time window of 0.7 min and an alignment time window of 20 min. Results were filtered for a minimal peptide length of seven amino acids. The resulting protein library was loaded into Perseus (version 1.6.15.0) for label-free quantification (LFQ) analysis. Data were filtered to remove proteins only identified by site as well as potential contaminants and reverse hits. We selected for proteins that were identified in all three replicates in at least one group, $\log_2$-transformed LFQ intensities, and imputed missing values on the basis of quantile regression imputation of left-censored data (QRILC) method using the imputeQRILC function of imputeLCMD package written for R.

The resulting LFQ intensities were used to calculate differential abundance (difference) of proteins compared to Tac0-BioID2, and profile plots of the resulting mean differences were used to highlight trends throughout groups. To control for endogenous biotinylation levels, we analyzed ratios of Tac0-BioID2–normalized LFQ values of TachAH-BioID2 constructs versus Tac0-BioID2–normalized LFQ values obtained for untransfected cells

$$\text{Abundance relative to Tac} = \text{LFQ}_{\text{TacAH}} - \text{`LFQ}_{\text{Tac}}$$

$$\text{Normalized abundance relative to pcDNA} = \frac{\text{LFQ}_{\text{TacAH}}}{\text{`LFQ}_{\text{Tac}}} - \frac{\text{LFQ}_{\text{pcDNA}}}{\text{`LFQ}_{\text{Tac}}}$$

## Immunoblotting

Protein lysates were mixed with 5× SDS–polyacrylamide gel electrophoresis loading buffer (50 mM DTT and 355 mM β-mercaptoethanol), boiled at 95°C for 5 min before being loaded into an Any-kD (Mini-ProTEAN TGX, Bio-Rad), and run at 115 V for 1 hour. The size-separated proteins were transferred to polyvinylidene difluoride membranes (Bio-Rad) for 10 min at 25 V on a trans-blot turbo transfer system (Bio-Rad) and blocked for 1 hour in 5% milk in wash buffer (PBS with 0.05% Tween 20). Membranes were incubated with primary antibodies (anti-FLAG M1 antibody) for 1 hour at 25°C or overnight at 4°C, washed three times for 15 min, and incubated with HRP-conjugated secondary anti-mouse antibodies for 30 min. Membranes were washed three times for 15 min before developing using either the SuperSignal ELISA Femto Substrate (Thermo Fisher Scientific) or ELC Prime Western Blotting system (Sigma-Aldrich) and captured with a cooled CCD camera.

## Gel-assisted GUV formation

The general procedure for gel-assisted GUV formation followed a previously published protocol (*56*). In brief, a 5% (w/w) solution of polyvinyl alcohol (PVA) (molecular weight above 146 kDa, Merck) was prepared by stirring PVA in 20 mM tris (pH 7.4) and 150 mM sucrose while heating to 90°C until appearing clear to the eye. We applied a thin film of 15 μl of PVA solution to a plasma-cleaned microscope coverslip (20 mm by 20 mm, Menzel-Gläser) and left the solution to dry for 30 min at 50°C. We spread 10 μl of lipids (1 mg/ml) on the dried PVA and evaporated the solvent for 60 min under vacuum. A lipid composition of (79.3 mol % DOPC:10 mol % DOPS:10 mol % cholesterol:0.5 mol % BODIPY-TR:0.3 mol % PEG-Biotin) dissolved in chloroform was used. Next, we applied 1 ml of growth buffer solution [5 mM Mops (pH 7.4), 20 mM NaCl, and 255 mM sucrose in water adjusted to 300 mosmol by addition of sucrose] and left GUVs swelling for 30 to 45 min at 20°C. After swelling period, GUVs were detached by gentle tipping against the bottom of the chamber and transferred to Eppendorf tubes using a P1000 pipette with a cut tip to decrease chance of bursting. The prepared GUV solution was used the earliest after a 15-min equilibration period and kept at 4°C for a maximum of 3 days.

## Pulling nanotubes from GUVs

The general procedure for pulling nanotubes followed a previously published protocol (*57*). In brief, we prepared micropipettes by pulling borosilicate glass capillaries (GC100-15, Harvard Apparatus) with a Sutter P-2000 (Sutter instruments). The tip was refined using a microforge, resulting in a final inner diameter of 5 to 7 μm, corresponding to ~$^1/_3$ of typical GUV diameter investigated. Before experiments, both the experimental chamber and the micropipette for micromanipulation of GUVs were passivated using a solution of highly pure β-casein (5 mg/ml; C6905, Sigma-Aldrich) in experimental buffer [20 mM Mops (pH 7.4), 100 mM NaCl, and 90 mM glucose in water adjusted to 310 mosmol by addition of glucose] and leaving the solution for more than 30 min to minimize the chance of GUVs adhering to the glass surface and bursting. After passivating, the experimental chamber was washed three times in experimental buffer, and a few microliters of streptavidin-coated polystyrene beads (3- to 3.4-μm diameter, SVP-30-5, Spherotech) were added to the chamber. During the passivating step, we prepared a mix of 1 μM Oregon Green–labeled peptide and 10% of the GUV solution prepared as described above in experimental buffer and let the mix incubate for 30 min before addition to the experimental chamber. We let the GUVs settle and deflate by leaving the buffer to evaporate for ~15 min, allowing them to be "floppy," and then sealed the experimental chamber using mineral oil. Aspiration pressure of the micromanipulation pipette was then equilibrated using a polystyrene bead before every tube pulling recording. We then aspirated a GUV, trapped a bead using optical tweezers, and positioned both at ~20 μm from the glass surface. Membrane tensions was relieved without losing the GUV from the micropipette, and the GUV was carefully positioned using a piezo-actuator in proximity to the bead to allow for streptavidin-biotin bonds to form. Careful separation of GUV and beads then allowed nanotube formation, and the aspiration pressure was increased to recreate an aspiration tongue. Movement of the bead was recorded using a bright-field microscope for a minute, followed by confocal imaging and recording of the water tank height position relative to equilibrium. This step was repeated multiple times at increasing aspiration pressure. Quantitative evaluation of membrane curvature sorting was then calculated as a sorting coefficient, *S*, given by

$$S = \frac{\dfrac{\text{Intensity}_{\text{Protein in tube}}}{\text{Intensity}_{\text{Protein in GUV}}}}{\dfrac{\text{Intensity}_{\text{Lipid in tube}}}{\text{Intensity}_{\text{Lipid in GUV}}}}$$

where $\text{Intensity}_{\text{Protein in tube}}$ and $\text{Intensity}_{\text{Protein in GUV}}$ represent the fluorescence intensities of proteins and $\text{Intensity}_{\text{Lipid in tube}}$ and

$Intensity_{Lipid\ in\ GUV}$ represent the fluorescence intensities of lipids on the tube and GUV, respectively. These intensities were calculated given the difference in summed intensities observed over a range of line scans analyzed for regions of interest for GUV and tube (Fig. 3H).

### Statistical analysis

Analysis was performed using GraphPad Prism software v6.01. Statistical comparisons across groups were done with a one-way analysis of variance (ANOVA) in the case of confocal microscopy data. Averages from flow cytometry data were analyzed with one-way ANOVA using Dunnett's correction for multiple comparisons, except for grouped data, as in the case of EE-mutants (Fig. 1C) and Dyngo treatment (fig. S13). Here, a two-way ANOVA with Šidák's or Tukey's correction for multiple comparisons was applied, unless stated otherwise. Linear regression was performed as standard, and goodness of fit was indicated with $R^2$ and $P$ values.

## Supplementary Materials

**This PDF file includes:**

Mathematical model "Acidification Kinetics Function"
Figs. S1 to S30
Tables S1 and S2
References

## REFERENCES AND NOTES


1. H. T. McMahon, E. Boucrot, Molecular mechanism and physiological functions of clathrin-mediated endocytosis. *Nat. Rev. Mol. Cell. Biol.* **12**, 517–533 (2011).
2. J. S. Bonifacino, L. M. Traub, Signals for sorting of transmembrane proteins to endosomes and lysosomes. *Annu. Rev. Biochem.* **72**, 395–447 (2003).
3. A. Sanger, J. Hirst, A. K. Davies, M. S. Robinson, Adaptor protein complexes and disease at a glance. *J. Cell Sci.* **132**, jcs222992 (2019).
4. H. T. McMahon, E. Boucrot, Membrane curvature at a glance. *J. Cell Sci.* **128**, 1065–1070 (2015).
5. B. Antonny, Mechanisms of membrane curvature sensing. *Annu. Rev. Biochem.* **80**, 101–123 (2011).
6. N. S. Hatzakis, V. K. Bhatia, J. Larsen, K. L. Madsen, P. Y. Bolinger, A. H. Kunding, J. Castillo, U. Gether, P. Hedegård, D. Stamou, How curved membranes recruit amphipathic helices and protein anchoring motifs. *Nat. Chem. Biol.* **5**, 835–841 (2009).
7. G. Drin, B. Antonny, Amphipathic helices and membrane curvature. *FEBS Lett.* **584**, 1840–1847 (2010).
8. J. Bockaert, J. P. Pin, Molecular tinkering of G protein-coupled receptors: An evolutionary success. *EMBO J.* **18**, 1723–1729 (1999).
9. A. S. Hauser, M. M. Attwood, M. Rask-Andersen, H. B. Schiöth, D. E. Gloriam, Trends in GPCR drug discovery: New agents, targets and indications. *Nat. Rev. Drug Discov.* **16**, 829–842 (2017).
10. K. Palczewski, T. Kumasaka, T. Hori, C. A. Behnke, H. Motoshima, B. A. Fox, I. Le Trong, D. C. Teller, T. Okada, R. E. Stenkamp, M. Yamamoto, M. Miyano, Crystal structure of rhodopsin : A G protein-coupled receptor. *Science* **289**, 739–746 (2000).
11. V. Isberg, S. Mordalski, C. Munk, K. Rataj, K. Harpsøe, A. S. Hauser, B. Vroling, A. J. Bojarski, G. Vriend, D. E. Gloriam, GPCRdb: An information system for G protein-coupled receptors. *Nucleic Acids Res.* **44**, D356–D364 (2016).
12. D. M. Rosenbaum, S. G. F. Rasmussen, B. K. Kobilka, The structure and function of G-protein-coupled receptors. *Nature* **459**, 356–363 (2009).
13. H. Zhang, H. Unal, H. Zhang, H. Unal, C. Gati, G. W. Han, W. Liu, N. A. Zatsepin, D. James, O. M. Yefanov, T. A. White, C. Wang, A. Ishchenko, Structure of the angiotensin receptor revealed by serial femtosecond crystallography. *Cell* **161**, 833–844 (2015).
14. J. Huynh, W. G. Thomas, M. I. Aguilar, L. K. Pattenden, Role of helix 8 in G protein-coupled receptors based on structure-function studies on the type 1 angiotensin receptor. *Mol. Cell. Endocrinol.* **302**, 118–127 (2009).
15. J. S. Bonifacino, P. Cosson, R. D. Klausner, Colocalized transmembrane determinants for ER degradation and subunit assembly explain the intracellular fate of TCR chains. *Cell* **63**, 503–513 (1990).
16. P. K. Tan, C. Waites, Y. Liu, D. E. Krantz, R. H. Edwards, A leucine-based motif mediates the endocytosis of vesicular monoamine and acetylcholine transporters. *J. Biol. Chem.* **273**, 17351–17360 (1998).
17. K. A. Neve, R. Qanbar, M. Bouvier, Role of palmitoylation/depalmitoylation reactions in G-protein-coupled receptor function. *Pharmacol. Ther.* **1**, 1–33 (2003).
18. S. Mostafapour, B. K. Kobilka, M. von Zastrow, Pharmacological sequestration of a chimeric beta 3/beta 2 adrenergic receptor occurs without a corresponding amount of receptor internalization. *Recept. Signal Transduct.* **6**, 151–163 (1996).
19. D. B. Heidorn, J. Trewhell, Comparison of the crystal and solution structures of calmodulin and troponin C. *Biochemistry* **27**, 909–915 (1988).
20. J. T. C. Branden, *Introduction to Protein Structure* (Garland Science, ed. 2, 1999).
21. M. Magdeleine, R. Gautier, P. Gounon, H. Barelli, S. Vanni, B. Antonny, A filter at the entrance of the Golgi that selects vesicles according to size and bulk lipid composition. *eLife* **5**, e16988 (2016).
22. B. Mesmin, G. Drin, S. Levi, M. Rawet, D. Cassel, J. Bigay, B. Antonny, Two lipid-packing sensor motifs contribute to the sensitivity of ArfGAP1 to membrane curvature. *Biochemistry* **46**, 1779–1790 (2007).
23. M. H. Høie, E. N. Kiehl, B. Petersen, M. Nielsen, O. Winther, H. Nielsen, J. Hallgren, P. Marcatili, NetSurfP-3.0: Accurate and fast prediction of protein structural features by protein language models and deep learning. *Nucleic Acids Res.* **50**, W510–W515 (2022).
24. R. A. Warren, F. A. Green, P. E. Stenberg, C. A. Enns, Distinct saturable pathways for the endocytosis of different tyrosine motifs. *J. Biol. Chem.* **273**, 17056–17063 (1998).
25. D. I. Kim, S. C. Jensen, K. A. Noble, B. Kc, K. H. Roux, K. Motamedchaboki, K. J. Roux, An improved smaller biotin ligase for BioID proximity labeling. *Mol. Biol. Cell* **27**, 1188–1196 (2016).
26. C. D. Go, J. D. R. Knight, A. Rajasekharan, B. Rathod, G. G. Hesketh, K. T. Abe, J. Y. Youn, P. Samavarchi-Tehrani, H. Zhang, L. Y. Zhu, E. Popiel, J. P. Lambert, É. Coyaud, S. W. T. Cheung, D. Rajendran, C. J. Wong, H. Antonicka, L. Pelletier, A. F. Palazzo, E. A. Shoubridge, B. Raught, A. C. Gingras, A proximity-dependent biotinylation map of a human cell. *Nature* **595**, 120–124 (2021).
27. M. Kaksonen, A. Roux, Mechanisms of clathrin-mediated endocytosis. *Nat. Rev. Mol. Cell Biol.* **19**, 313–326 (2018).
28. M. Shafaq-Zadah, E. Dransart, L. Johannes, Clathrin-independent endocytosis, retrograde trafficking, and cell polarity. *Curr. Opin. Cell Biol.* **65**, 112–121 (2020).
29. R. G. Parton, Caveolae: Structure, function, and relationship to disease. *Annu. Rev. Cell Dev. Biol.* **34**, 111–136 (2018).
30. A. Casamento, E. Boucrot, Molecular mechanism of fast endophilin-mediated endocytosis. *Biochem. J.* **477**, 2327–2345 (2020).
31. L. M. Traub, Regarding the amazing choreography of clathrin coats. *PLOS Biol.* **9**, e1001037 (2011).
32. S. Polo, S. Sigismund, M. Faretta, M. Guidi, M. R. Capua, G. Bossi, H. Chen, P. De Camilli, P. P. Di Fiore, A single motif responsible for ubiquitin recognition and monoubiquitination in endocytic proteins. *Nature* **416**, 451–455 (2002).
33. L. Christ, C. Raiborg, E. M. Wenzel, C. Campsteijn, H. Stenmark, Cellular functions and molecular mechanisms of the ESCRT membrane-scission machinery. *Trends Biochem. Sci.* **42**, 42–56 (2017).
34. C. J. Merrifield, D. Perrais, D. Zenisek, Coupling between clathrin-coated-pit invagination, cortactin recruitment, and membrane scission observed in live cells. *Cell* **121**, 593–606 (2005).
35. M. J. Taylor, D. Perrais, C. J. Merrifield, A high precision survey of the molecular dynamics of mammalian clathrin-mediated endocytosis. *PLOS Biol.* **9**, e1000604 (2011).
36. K. S. Stroh, H. J. Risselada, Quantifying membrane curvature sensing of peripheral proteins by simulated buckling and umbrella sampling. *J. Chem. Theory Comput.* **17**, 5276–5286 (2021).
37. J. Heuser, L. Evans, Three-dimensional visualization of coated vesicle formation in fibroblasts. *J. Cell Biol.* **84**, 560–583 (1980).
38. P. M. Dijkman, J. C. Muñoz-García, S. R. Lavington, P. S. Kumagai, R. I. dos Reis, D. Yin, P. J. Stansfeld, A. J. Costa-Filho, A. Watts, Conformational dynamics of a G protein–coupled receptor helix 8 in lipid membranes. *Sci. Adv.* **6**, eaav8207 (2020).
39. J. H. Schmidt, M. Perslev, L. Bukowski, M. Stoklund, F. Herborg, R. Herlo, K. Lindegaard Madsen, Constitutive internalization across therapeutically targeted GPCRs correlates with constitutive activity. *Basic Clin. Pharmacol. Toxicol.* **126**, 116–121 (2020).
40. L. P. T. Herrera, S. N. Andreassen, J. Caroli, I. Rodríguez-Espigares, A. A. Kermani, G. M. Keseru, A. J. Kooistra, G. Pándy-Szekeres, D. E. Gloriam, GPCRdb in 2025: Adding odorant receptors, data mapper, structure similarity search and models of physiological ligand complexes. *Nucleic Acids Res.* **53**, D425–D435 (2025).
41. M. M. Rosenkilde, N. Tsutsumi, J. M. Knerr, D. F. Kildedal, K. C. Garcia, Viral G protein–coupled receptors encoded by β- and γ-herpesviruses. *Annu. Rev. Virol.* **9**, 329–351 (2022).
42. A. Fletcher-Jones, K. L. Hildick, A. J. Evans, Y. Nakamura, K. A. Wilkinson, J. M. Henley, The C-Terminal helix 9 motif in rat cannabinoid receptor type 1 regulates axonal trafficking and surface expression. *eLife* **8**, e44252 (2019).
43. K. H. Ahn, A. Nishiyama, D. F. Mierke, D. A. Kendall, Hydrophobic residues in helix 8 of cannabinoid receptor 1 are critical for structural and functional properties. *Biochemistry* **49**, 502 (2010).

44. V. Macarelli, E. C. Harding, D. C. Gershlick, F. T. Merkle, A short sequence targets transmembrane proteins to primary cilia. *Cells* **13**, 1156 (2024).
45. S. Erdogmus, U. Storch, L. Danner, J. Becker, M. Winter, N. Ziegler, A. Wirth, S. Offermanns, C. Hoffmann, T. Gudermann, M. Mederos y Schnitzler, Helix 8 is the essential structural motif of mechanosensitive GPCRs. *Nat. Commun.* **10**, 5784 (2019).
46. G. Wang, L. Jiang, J. Wang, J. Zhang, F. Kong, Q. Li, Y. Yan, S. Huang, Y. Zhao, L. Liang, J. Li, N. Sun, Y. Hu, W. Shi, G. Deng, P. Chen, L. Liu, X. Zeng, G. Tian, Z. Bu, H. Chen, C. Li, The G protein-coupled receptor FFAR2 promotes internalization during influenza A virus entry. *J. Virol.* **94**, e01707-19 (2020).
47. M. Z. Li, S. J. Elledge, SLIC: A method for sequence- and ligation-independent cloning. *Methods Mol. Biol.* **852**, 51–59 (2012).
48. C. T. Rueden, J. Schindelin, M. C. Hiner, B. E. DeZonia, A. E. Walter, E. T. Arena, K. W. Eliceiri, ImageJ2: ImageJ for the next generation of scientific image data. *BMC Bioinformatics* **18**, 529 (2017).
49. F. Pedregosa, G. Varoquaux, A. Gramfort, V. Michel, B. Thirion, O. Grisel, M. Blondel, P. Prettenhofer, R. Weiss, V. Dubourg, J. Vanderplas, A. Passos, D. Cournapeau, M. Brucher, M. Perrot, E. Duchesnay, Scikit-learn: Machine learning in python. *J. Mach. Learn. Res.* **12**, 2825–2830 (2011).
50. H. M. Maric, T. J. Hausrat, F. Neubert, N. O. Dalby, S. Doose, M. Sauer, M. Kneussel, K. Strømgaard, Gephyrin-binding peptides visualize postsynaptic sites and modulate neurotransmission. *Nat. Chem. Biol.* **13**, 153–160 (2017).
51. N. R. Christensen, C. P. Pedersen, V. Sereikaite, J. N. Pedersen, M. Vistrup-Parry, A. T. Sørensen, D. Otzen, K. Teilum, K. L. Madsen, K. Strømgaard, Bidirectional protein–protein interactions control liquid–liquid phase separation of PSD-95 and its interaction partners. *iScience* **25**, 103808 (2022).
52. L. B. Hansen, S. Buus, C. Schafer-Nielsen, Identification and mapping of linear antibody epitopes in human serum albumin using high-density peptide arrays. *PLOS ONE* **8**, e68902 (2013).
53. D. Baddeley, M. B. Cannell, C. Soeller, Three-dimensional sub-100 nm super-resolution imaging of biological samples using a phase ramp in the objective pupil. *Nano Res* **4**, 589–598 (2011).
54. H. Babcock, Y. M. Sigal, X. Zhuang, A high-density 3D localization algorithm for stochastic optical reconstruction microscopy. *Opt. Nanoscopy* **1**, 10.1186/2192-2853-1-6 (2012).
55. S. Tyanova, T. Temu, J. Cox, The MaxQuant computational platform for mass spectrometry-based shotgun proteomics. *Nat. Protoc.* **11**, 2301–2319 (2016).
56. A. Weinberger, F. C. Tsai, G. H. Koenderink, T. F. Schmidt, R. Itri, W. Meier, T. Schmatko, A. Schröder, C. Marques, Gel-assisted formation of giant unilamellar vesicles. *Biophys. J.* **105**, 154–164 (2013).
57. C. Prévost, F. C. Tsai, P. Bassereau, M. Simunovic, Pulling membrane nanotubes from giant unilamellar vesicles. *J. Vis. Exp.* **2017**, 56086 (2017).
58. R. Gautier, D. Douguet, B. Antonny, G. Drin, HELIQUEST: A web server to screen sequences with specific α-helical properties. *Bioinformatics* **24**, 2101–2102 (2008).
59. J. Jumper, R. Evans, A. Pritzel, T. Green, M. Figurnov, O. Ronneberger, K. Tunyasuvunakool, R. Bates, A. Žídek, A. Potapenko, A. Bridgland, C. Meyer, S. A. A. Kohl, A. J. Ballard, A. Cowie, B. Romera-Paredes, S. Nikolov, R. Jain, J. Adler, T. Back, S. Petersen, D. Reiman, E. Clancy, M. Zielinski, M. Steinegger, M. Pacholska, T. Berghammer, S. Bodenstein, D. Silver, O. Vinyals, A. W. Senior, K. Kavukcuoglu, P. Kohli, D. Hassabis, Highly accurate protein structure prediction with AlphaFold. *Nature* **596**, 583–589 (2021).
60. K. T. Chang, J. Guo, A. Di Ronza, M. Sardiello, Aminode: Identification of evolutionary constraints in the human proteome. *Sci. Rep.* **8**, 1357 (2018).
61. C. Sudlow, J. Gallacher, N. Allen, V. Beral, P. Burton, J. Danesh, P. Downey, P. Elliott, J. Green, M. Landray, B. Liu, P. Matthews, G. Ong, J. Pell, A. Silman, A. Young, T. Sprosen, T. Peakman, R. Collins, UK Biobank: An open access resource for identifying the causes of a wide range of complex diseases of middle and old age. *PLOS Med.* **12**, e1001779 (2015).
62. A. Bateman, UniProt: A worldwide hub of protein knowledge. *Nucleic Acids Res.* **47**, D506–D515 (2019).
63. W. K. Kroeze, M. F. Sassano, X. P. Huang, K. Lansu, J. D. McCorvy, P. M. Giguère, N. Sciaky, B. L. Roth, PRESTO-Tango as an open-source resource for interrogation of the druggable human GPCRome. *Nat. Struct. Mol. Biol.* **22**, 362–369 (2015).
64. A. S. Hauser, C. Avet, C. Normand, A. Mancini, A. Inoue, M. Bouvier, D. E. Gloriam, Common coupling map advances GPCR-G protein selectivity. *eLife* **11**, e74107 (2022).


**Acknowledgments:** We acknowledge the Proteomics Research Infrastructure, Core Facility for Integrated Microscopy and Flow Cytometry and Single Cell Analysis facilities at the University of Copenhagen. Further, we would like to thank N. Khadim for technical assistance. **Funding:** This work was supported by the following grants: Danish Research Counsil (DFF), Medical Sciences, FP 1 (2034-00395A) (to K.L.M.); Lundbeckfonden, Lundbeck Foundation Experiment (R324-2019-1806) (to K.L.M.); Lundbeck Foundation Post Doc grant (R347-2020-2339) (to A.H.L.); Labex Cell(n)Scale (ANR-11-LABX0038) (to P.B.); ParisSciences et Lettres (ANR-10-IDEX-0001-02) (to P.B.); and Fondation pour la Recherche Médicale (FRM EQU202003010307) (to P.B.). **Author contributions:** Conceptualization: K.L.M., U.G., J.H.S., and R.H. Methodology: K.L.M., J.H.S., R.H., N.R.C., A.L.E., M.D.L., J.R., A.H.L., Mi.S., M.P., K.A.A., C.K.H., J.P.C., D.P., P.B., and A.S.H. Investigation: K.L.M., J.H.S., R.H., J.R., A.H.L., Mi.S., M.P., K.A.A., M.D.L., and A.L.E. Visualization: K.L.M., J.H.S., R.H., J.R., A.H.L., Mo.S., T.T.E.N., and D.P. Funding acquisition: K.L.M., U.G., A.H.L., P.B., and D.P.. Project administration: K.L.M. Supervision: K.L.M., D.P., P.B., and C.K.H. Writing—original draft: K.L.M., J.H.S., and R.H. Writing—review and editing: K.L.M., J.H.S., R.H., J.R., F.H., and A.H.L. **Competing interests:** The authors declare that they have no competing interests. **Data and materials availability:** All data needed to evaluate the conclusions in the paper are present in the paper and/or the Supplementary Materials.

Submitted 6 December 2024
Accepted 11 July 2025
Published 13 August 2025
10.1126/sciadv.adv1499